

Single-energy partial wave analysis for pion photoproduction with fixed- t analyticity

H. Osmanović,^{1,*} M. Hadžimehmedović,¹ R. Omerović,¹ J. Stahov,^{1,2}
V. Kashevarov,^{3,4} M. Ostrick,³ L. Tiator,³ and A. Švarc^{5,6}

¹*University of Tuzla, Faculty of Natural Sciences and Mathematics,
Urfeta Vejzagića 4, 75000 Tuzla, Bosnia and Herzegovina*

²*European University "Kallos", Maršala Tita 2A-2B, 75000 Tuzla, Bosnia and Herzegovina*

³*Institut für Kernphysik, Johannes Gutenberg-Universität Mainz, D-55099 Mainz, Germany*

⁴*P. N. Lebedev Physical Institute, 119991 Moscow, Russia*

⁵*Rudjer Bošković Institute, Bijenička cesta 54, P.O. Box 180, 10002 Zagreb, Croatia*

⁶*Tesla Biotech, Mandlova 7, 10002 Zagreb, Croatia*

(Dated: November 25, 2021)

Experimental data for pion photoproduction including differential cross sections and various polarization observables from four reaction channels, $\gamma p \rightarrow \pi^0 p$, $\gamma p \rightarrow \pi^+ n$, $\gamma n \rightarrow \pi^- p$ and $\gamma n \rightarrow \pi^0 n$ from threshold up to $W = 2.2$ GeV have been used in order to perform a single-energy partial wave analysis with minimal model dependence by imposing constraints from unitarity and fixed- t analyticity in an iterative procedure. Reaction models were only used as starting point in the very first iteration. We demonstrate that with this procedure partial wave amplitudes can be obtained which show only a minimal dependence on the initial model assumptions.

The analysis has been obtained in full isospin, and the Watson theorem is enforced for energies below $W = 1.3$ GeV but is even fulfilled up to $W \approx 1.6$ GeV in many partial waves. Electromagnetic multipoles $E_{\ell\pm}$ and $M_{\ell\pm}$ are presented and discussed for S, P, D and F -waves.

arXiv:2107.06513v1 [nucl-th] 14 Jul 2021

* hedim.osmanovic@unitz.ba

I. INTRODUCTION

Meson-nucleon scattering and meson photoproduction have been extensively studied during the last decades in a comprehensive joint program between experiment and theory. The objective of this effort is the exploration and determination of all relevant characteristics of light baryon resonances, N^* and Δ^* , i.e. pole positions, decay widths, and branching ratios. The pion is the lightest meson and couples strongly to many of these excited states. Therefore, pion scattering and photoproduction of pions are of central importance for all analyses which aim to identify and characterize the excited states of nucleons. A reliable description and understanding of pion photoproduction is a prerequisite also for the analysis and interpretation of other final states.

Experimentally, major progress was made due to the availability of high intensity polarized beams and polarized targets in combination with 4π detector systems. In experiments at ELSA, GRAAL, JLab and MAMI the spin dependence of pion production has been explored with unprecedented quality and quantity.

On theory side, single or multi-channel models were developed and used to interpret the data in terms of resonance parameters. These approaches are called energy-dependent (ED) analyses because the energy dependence of amplitudes is parameterized in terms of resonant and non-resonant contributions. Resonance properties can be related to the parameters of such models and are estimated by fits to the data. In practical calculations compromises are necessary between the compliance of fundamental constraints like analyticity, unitarity and crossing symmetry on the one side, and computing power necessary for important systematic studies on the other side. In general, the extracted resonance parameters vary from model to model. A recent comparison of the prominent ED models (Bonn-Gatchina (BnGa)-[1], Jülich-Bonn (JüBo)-[2], George Washington University (GW-SAID)-[3], and Mainz (MAID)-[4]) and the impact of new polarization data has been published in Ref. [5].

In so called energy-independent or single-energy (SE) analyses a truncated partial wave or multipole expansion is fitted to the measured angular distributions independently at each individual energy bin without using a reaction model. The interpretation of the obtained multipole amplitudes however is hampered by phase ambiguities which cannot be resolved by high-quality experimental data alone [6–8]. For each bin in energy and angle one overall phase remains undetermined. In Ref. [9] it has been demonstrated that a unique SE multipole analysis is not possible without some theoretical phase constraints.

In Refs. [10, 11] we developed a method to impose analyticity of the reactions amplitudes in the Mandelstam variable s at a fixed value of the variable t in an iterative procedure. A reaction model is only necessary as a starting point in the very first iteration. We applied this method to the $\gamma p \rightarrow \eta p$ and $\gamma p \rightarrow \pi^0 p$ reactions and demonstrated that indeed single energy multipole amplitudes with meaningful energy dependence can be obtained. Remaining ambiguities were traced back to limitations in the experimental data base and different overall phases of the initial reaction models. In the case of pion production, however, a complete partial wave analysis necessitates the isospin decomposition of each multipole amplitude because both, excitations with isospin $I = 1/2$ (N^*) and $I = 3/2$ (Δ^*), can contribute. Such an analysis is the objective of the present paper. It requires the simultaneous analysis of at least three of the four possible reactions, $\gamma p \rightarrow \pi^0 p$, $\gamma p \rightarrow \pi^+ n$, $\gamma n \rightarrow \pi^- p$, and $\gamma n \rightarrow \pi^0 n$. At low energies, unitarity in the form of Watson's theorem [12] relates the phases of isospin multipoles to the corresponding phases in πN scattering which provides powerful constraints to resolve the phase ambiguity in a model independent way. This is an advantage compared to our previous study in Ref. [11].

The paper is organized as follows. In section II we briefly describe the formalism. In section III we comment on the experimental data that were used in our analysis and present the single-energy multipoles for different starting solutions. We compare our results with experimental data and with partial wave analyses from other groups, Bonn-Gatchina, GWU/SAID and MAID. Finally, in the appendix we give basic formula for kinematics, polarization observables and partial wave amplitudes in different isospin representations.

II. FORMALISM

In this paper, we apply the fixed- t analyticity constraining method for single-energy partial wave analysis (SE PWA) in pion photoproduction. The method was developed previously and applied in η photoproduction on the proton [10]. Later on, the method was applied in SE PWA of π^0 photoproduction on the proton, considering π^0 as a "light η meson" [11]. All details about the method are given in these two papers. The isospin in the final state in η photoproduction is $1/2$, while in pion photoproduction it is either $1/2$ or $3/2$. Therefore, each of four invariant amplitudes $A_i(\nu, t)$ (for kinematics see appendix A) describing photoproduction of pseudoscalar mesons on nucleons, can be decomposed into three isospin amplitudes (see appendix D).

In order to describe all four channels $N(\gamma, \pi)N$ ($p(\gamma, \pi^0)p$, $p(\gamma, \pi^+)n$, $n(\gamma, \pi^-)p$, $n(\gamma, \pi^0)n$), one has to determine twelve instead of only four amplitudes in η photoproduction, what makes the whole analysis more complicated

and numerically much more demanding. From the other side, much more experimental data are available in pion photoproduction and allow reliable solutions for electric and magnetic multipoles.

The method consists of two separate analyses, the fixed- t amplitude analysis (FT AA) and the single-energy partial wave analysis (SE PWA). The two analyses are coupled in such a way that the results from FT AA are used as a constraint in SE PWA and vice versa in an iterative procedure. It has not been proven, but it is extensively tested in πN elastic, fixed- t constrained SE PWA [13], and since then recommended for other processes.

Step 1: Constrained FT AA is performed by minimizing the form

$$X^2 = \chi_{FTdata}^2 + \chi_{cons}^2 + \Phi_{conv}, \quad (1)$$

$$\begin{aligned} \chi_{cons}^2 = & q_{cons} \sum_{iso=1}^3 \sum_{k=1}^4 \sum_{i=1}^{N^E} \left[\frac{\text{Re } H_{iso,k}(W_i, t)^{fit} - \text{Re } H_{iso,k}(W_i, t)^{cons}}{\epsilon_{iso,k,i}^{\text{Re}}} \right]^2 \\ & + q_{cons} \sum_{iso=1}^3 \sum_{k=1}^4 \sum_{i=1}^{N^E} \left[\frac{\text{Im } H_{iso,k}(W_i, t)^{fit} - \text{Im } H_{iso,k}(W_i, t)^{cons}}{\epsilon_{iso,k,i}^{\text{Im}}} \right]^2 \end{aligned} \quad (2)$$

$H_{iso,k}^{cons}(W_i, t)$ are helicity amplitudes from SE PWA in the previous iteration, iso stands for three isospin combinations $(+, -, 0)$, and $k = 1, \dots, 4$ for helicity amplitudes in photoproduction of pseudoscalar mesons on the nucleon. In a first iteration, $H_{iso,k}^{cons}$ are calculated from the initial PWA solution (BnGa2019, SAID-M19, MAID2007). $H_{iso,k}^{fit}(W_i, t)$ are values of helicity amplitudes $H_{iso,k}$ calculated from coefficients in Pietarinen's expansions, which are parameters of the fit. N^E is the number of energies for a given value of t , and q_{cons} is an adjustable weight factor. $\epsilon_{iso,k,i}^{\text{Re}}$ and $\epsilon_{iso,k,i}^{\text{Im}}$ are errors of real and imaginary parts of the corresponding helicity amplitudes. In our analysis we take $\epsilon_{iso,k,i}^{\text{Re}} = \epsilon_{iso,k,i}^{\text{Im}} = 1$. Φ_{conv} is a Pietarinen's convergence test function, for details see Ref. [10].

Step 2: Constrained SE PWA is performed by minimizing the form

$$X^2 = \chi_{SEdata}^2 + \chi_{FT}^2 + \chi_{unitarity}^2 + \chi_{Born}^2 + \Phi_{trunc} \quad (3)$$

$$\begin{aligned} \chi_{FT}^2 = & q \sum_{iso=1}^3 \sum_{k=1}^4 \sum_{i=1}^{N^C} \left[\frac{\text{Re } H_{iso,k}(\theta_i, W)^{cons} - \text{Re } H_{iso,k}(\theta_i, W)^{fit}}{\epsilon_{iso,k,i}^{\text{Re}}} \right]^2 \\ & + q \sum_{iso=1}^3 \sum_{k=1}^4 \sum_{i=1}^{N^C} \left[\frac{\text{Im } H_{iso,k}(\theta_i, W)^{cons} - \text{Im } H_{iso,k}(\theta_i, W)^{fit}}{\epsilon_{iso,k,i}^{\text{Im}}} \right]^2 \end{aligned} \quad (4)$$

N^C is the number of angles for a given energy W and the values θ_i are obtained for a corresponding value of t using Eq. (A15). $H_{iso,k}^{cons}(\theta_i, W)$ are helicity amplitudes from FT AA in the previous iteration, $H_{iso,k}^{fit}(\theta_i, W)$ are values of helicity amplitudes $H_{iso,k}$ calculated from multipoles, which are parameters of the fit. Multipoles with isospin $I = 1/2$, and $I = 3/2$ are used. q is an adjustable weight factor. As in the first step, $\epsilon_{iso,k,i}^{\text{Re}}$ and $\epsilon_{iso,k,i}^{\text{Im}}$ are errors of real and imaginary parts of the corresponding helicity amplitudes. Again, we take $\epsilon_{iso,k,i}^{\text{Re}} = \epsilon_{iso,k,i}^{\text{Im}} = 1$. Φ_{trunc} makes a soft cutoff of higher partial waves and is effective at low energies, for details see Ref. [10]. According to unitarity (Watson's theorem [14]), phases of multipoles in pion photoproduction are equal to corresponding phases of πN partial waves up to $n\pi$:

$$\begin{aligned} (\delta_{\ell\pm}^I)_{\gamma,\pi} &= (\delta_{\ell\pm}^I)_{\pi N} + n\pi \\ \tan \left((\delta_{\ell\pm}^I)_{\gamma,\pi} \right) &= \tan \left((\delta_{\ell\pm}^I)_{\pi N} + n\pi \right) = \tan \left((\delta_{\ell\pm}^I)_{\pi N} \right) \\ \text{Im} (T_{\ell\pm}^I) &= \text{Re} (T_{\ell\pm}^I) \tan \left((\delta_{\ell\pm}^I)_{\pi N} \right) \end{aligned} \quad (5)$$

$T_{\ell\pm}^I$ and $\delta_{\ell\pm}^I$ stand for electric and magnetic multipoles with angular momentum $J = \ell \pm \frac{1}{2}$ and isospin I and their phases, and $(\delta_{\ell\pm}^I)_{\pi N}$ denotes corresponding πN phase. Term $\chi_{unitarity}^2$ is introduced to impose unitarity at low energies. It is defined as follows:

$$\chi_{unitarity}^2 = q_u \left[\text{Im} (T_{\ell\pm}^I) - \text{Re} (T_{\ell\pm}^I) \tan \left((\delta_{\ell\pm}^I)_{\pi N} \right) \right]^2, \quad (6)$$

where q_u is an adjustable weight factor. Above 1.4 GeV, q_u is smoothly truncated to zero at 1.6 GeV. Especially for pion photoproduction we also added a constraint to the Born terms, that appeared in any previous model dependent analysis as the most important aspect of pion photoproduction besides the excitation of the $\Delta(1232)$ resonance. The Born constraint is used up to 1.3 GeV

$$\chi_{Born}^2 = q_b \sum_{iso=1}^3 \sum_{\ell=1}^{\ell_{max}} (\text{Re}T_{iso,\ell} - T_{Born\ iso,\ell})^2. \quad (7)$$

Step 3: Use multipoles obtained in step 2 and calculate helicity amplitudes, which serve as a constraint in step 1.

χ_{FTdata}^2 and χ_{SEdata}^2 are standard χ^2 functions calculating the weighted deviations between theory and experiment. An iterative minimization scheme which accomplishes point-to-point continuity in energy is given in Fig. 1.

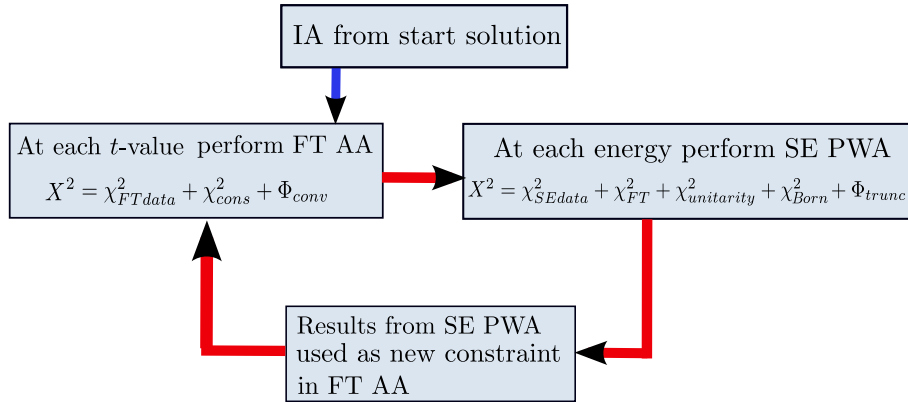


FIG. 1: Iterative minimization scheme which achieves point-to-point continuity in energy using fixed- t analyticity as a constraint. (IA: invariant amplitudes, FT AA: fixed- t amplitude analysis, SE PWA: single-energy partial wave analysis)

III. RESULTS

A. Data base for pion photoproduction

For our analysis, we used pion photoproduction data with $W < 2200$ MeV and $-1.00 \text{ GeV}^2 < t < -0.005 \text{ GeV}^2$ in three reaction channels. The largest data set exists for the $\gamma p \rightarrow \pi^0 p$ reaction. Over the past 70 years, more than 200 experimental papers for 10 independent observables were published for this reaction, see SAID data base [15]. However, the majority of experimental data were obtained during the last 20 years by the A2 Collaboration at Mainz Microtron MAMI (Mainz, Germany), the CBELSA/TAPS Collaboration at Electron Stretcher and accelerator ELSA (Bonn, Germany), the GRAAL Collaboration at European Synchrotron Radiation Facility (Grenoble, France), and the CLAS Collaboration at Thomas Jefferson National Accelerator Facility (Virginia, USA). We have not included in our fit the beam-recoil observables C_x and C_z , because of the small kinematic coverage and large uncertainties. A summary for the other 8 observables: unpolarized differential cross section ($\sigma_0 = d\sigma/d\Omega$), photon asymmetry (Σ), target asymmetry (T), recoil asymmetry (P), photon helicity asymmetry E , and double beam-target polarization asymmetries (F , G , H) is given in Table I and in Fig. 2. For the differential cross sections we used only the latest high precision data. Instead of the F asymmetry at low energies, $W < 1300$ MeV, we used polarized differential cross section, $F\sigma_0$, which was measured directly in this low-energy region.

TABLE I: Experimental data for $\pi^0 p$ channel used in our SE PWA. N is number of data points with $-1.00 \text{ GeV}^2 < t < -0.005 \text{ GeV}^2$.

Obs	N	W[MeV]	Reference
σ_0	600	1075 – 1136	A2MAMI-2013 [16]
	6451	1136 – 1894	A2MAMI-2015 [17]
	283	1465 – 2200	CLAS-2007 [18]
	216	1581 – 2200	CBELSA/TAPS-2011 [19]
Σ	528	1074 – 1215	A2MAMI-2013 [16]
	357	1150 – 1310	A2MAMI-2006 [20]
	296	1384 – 1910	GRAAL-2005 [21]
	214	1622 – 1998	CBELSA/TAPS-2010 [22]
	878	1201 – 2200	Ref. [23]
T	4410	1078 – 1291	A2MAMI-2015 [24]
	371	1295 – 1895	A2MAMI-2016 [25]
	157	1462 – 1620	CBELSA/TAPS-2014 [26]
	330	1291 – 2196	Ref. [27]
P	157	1462 – 1620	CBELSA/TAPS-2014 [26]
	532	1201 – 2200	Ref. [28]
E	413	1141 – 1870	A2MAMI-2015 [29]
	315	1426 – 2200	CBELSA/TAPS-2014 [30]
F	371	1295 – 1895	A2MAMI-2016 [25]
$F\sigma_0$	4500	1074 – 1291	A2MAMI-2015 [31]
G	3	1232	A2MAMI-2005 [32]
	318	1430 – 1727	CBELSA/TAPS-2012 [33]
	54	1232 – 2200	Ref. [34]
H	157	1462 – 1620	CBELSA/TAPS-2014 [26]
	50	1822 – 2200	Ref. [34]

For the $\gamma p \rightarrow \pi^+ n$ reaction we use 6 measured observables. In this case, the data base is still dominated by older measurements before the year 2000. More recent data exist only for σ_0 and Σ . We use the full database in our analysis. A summary is given in Table II and in Fig. 3.

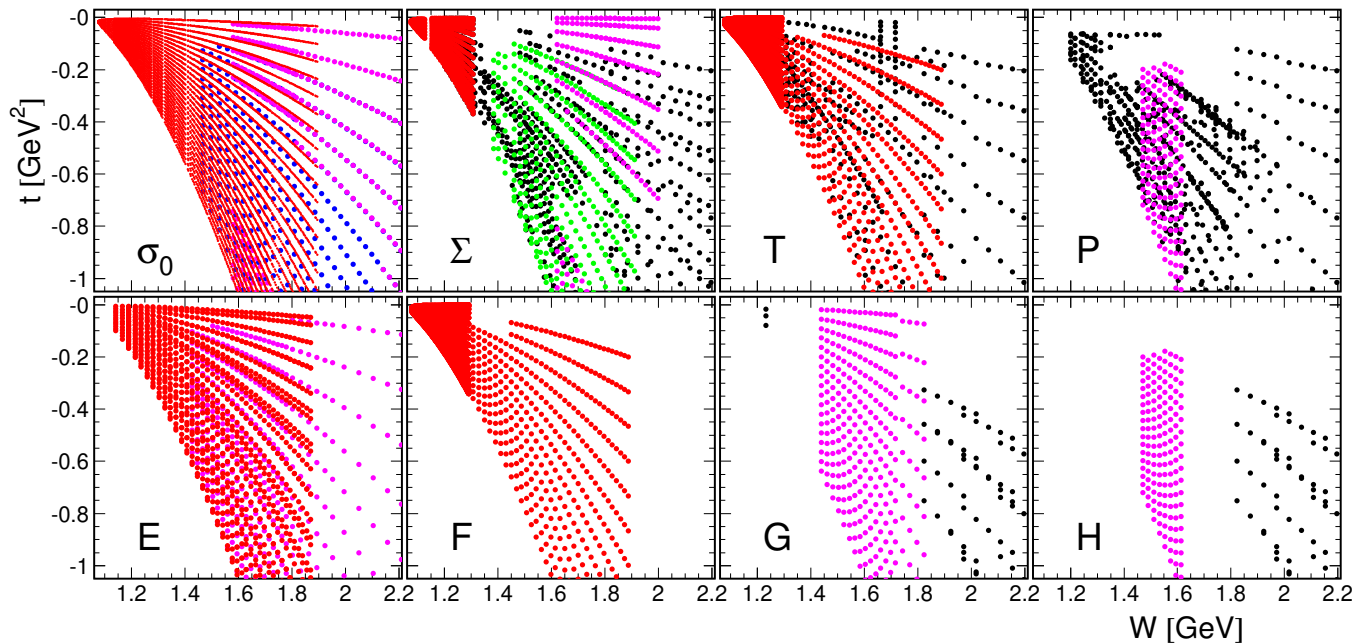


FIG. 2: Experimental data for $\pi^0 p$ channel used in our SE PWA are shown in W - t diagrams. The label in the lower left corner of each panel is the name of the observable. Different colors for the data points correspond to the collaborations: A2MAMI (red), CB/ELSA (magenta), CLAS (blue), GRAAL (green). Black points correspond to the Refs. [23], [27], [28], [34].

TABLE II: Experimental data for $\pi^+ n$ channel used in our SE PWA. All notations as in Table I.

<i>Obs</i>	<i>N</i>	<i>W</i> [MeV]	Reference
σ_0	129	1178 – 1313	A2MAMI-2004 [35]
	204	1323 – 1533	A2MAMI-2006 [36]
	250	1497 – 2200	CLAS-2009 [37]
	953	1481 – 2200	Ref. [38]
Σ	755	1201 – 2200	Ref. [39]
	153	1543 – 1901	GRAAL-2002 [40]
	195	1723 – 2093	CLAS-2014 [41]
T	597	1201 – 2200	Ref. [42]
P	237	1201 – 2200	Ref. [43]
G	85	1217 – 2097	Ref. [44]
H	126	1217 – 2052	Ref. [45]

TABLE III: Experimental data for $\pi^- p$ channel used in our SE PWA. All notations as in Table I.

<i>Obs</i>	<i>N</i>	<i>W</i> [MeV]	Reference
σ_0	746	1179 – 1798	Ref. [46]
	882	1179 – 2110	inverse data [47]
	126	1203 – 1318	A2MAMI-2012 [48]
	326	1690 – 2200	CLAS-2012 [49]
Σ	203	1188 – 2019	Ref. [50]
	99	1516 – 1894	CLAS-2014 [51]
T	104	1187 – 2065	Ref. [52]
P	68	1201 – 1764	Ref. [53]

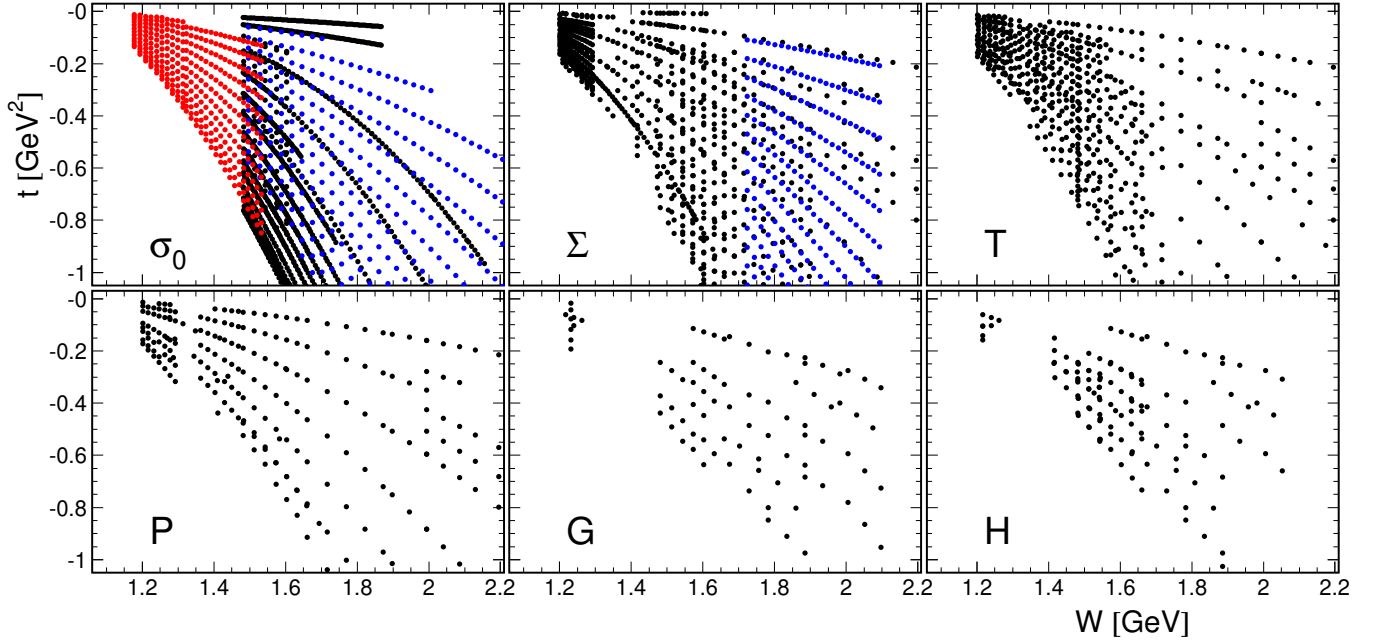


FIG. 3: Experimental data for π^+n channel used in our SE PWA. Notations as in Fig. 2. Black points correspond to the Refs. [38], [39], [42]-[45].

For the $\gamma n \rightarrow \pi^-p$ reaction we use 4 observables. A summary is given in Table III and in Fig. 4. As for $\gamma p \rightarrow \pi^+n$ reaction, data which have been measured before the year 2000 dominate and we used the full world data base. Beside direct measurements with deuteron target (old and new data), which should be corrected for Fermi motion and final state interactions, we have also data from inverse reaction $\pi^-p \rightarrow \gamma n$ (inverse data). It should be noted that data obtained from the inverse reaction are in a good agreement with the deuteron data.

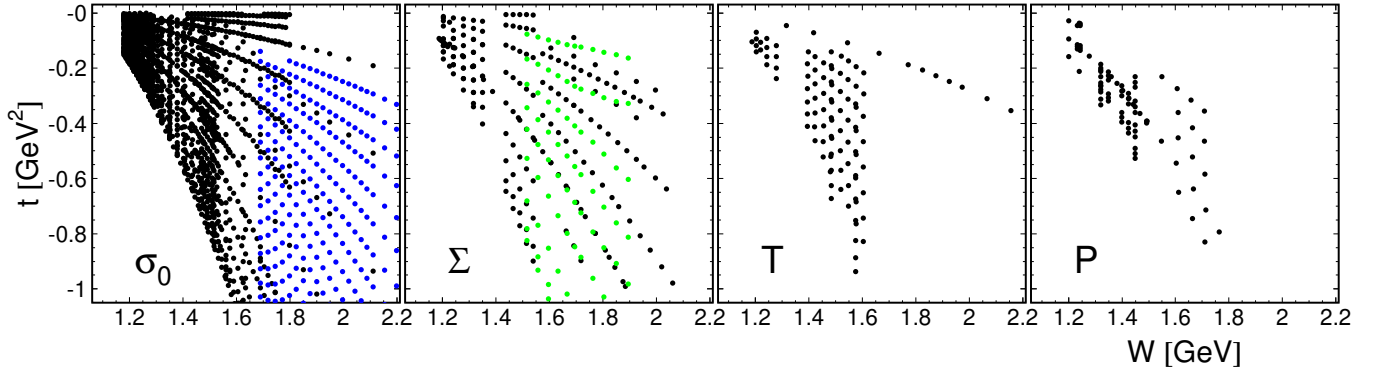


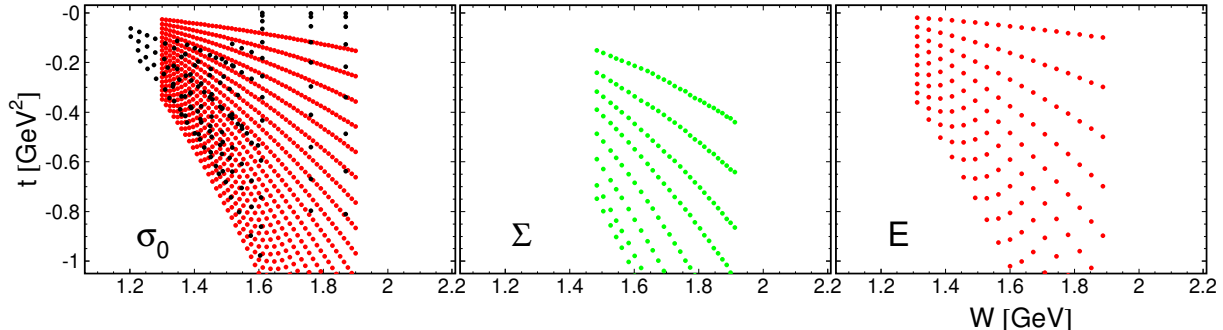
FIG. 4: Experimental data for π^-p channel used in our SE PWA. Notations as in Fig. 2. Black points correspond to the Refs. [46], [47], [50], [52], [53].

The data set for the $\gamma n \rightarrow \pi^0n$ reaction is smallest in comparison to other channels. A summary is given in Table IV and in Fig. 5. We have data only for three observables: σ_0 , Σ , and E . The data for this reaction were obtained from quasi-free scattering of neutrons bound in light nuclear targets and require corrections for Fermi motion and final state interactions. This adds additional systematic uncertainties to data. It should be noted that for the decomposition of all isospin multipoles $A^{(3/2)}$, $A_p^{(1/2)}$, and $A_n^{(1/2)}$ we only need a subset of three out of the four possible $\gamma N \rightarrow \pi N$ reactions. Therefore, we did not use the π^0n data set in our fit. Nevertheless, we compare our results also with data in this channel.

In general, there is a hierarchy of precision depending on the polarization degrees of freedom used in the experiment. The highest precision was achieved in measurements of the unpolarized differential cross section of $\gamma p \rightarrow \pi^0p$ at MAMI

TABLE IV: Experimental data for $\pi^0 n$ channel. All notations as in Table I.

<i>Obs</i>	<i>N</i>	<i>W</i> [MeV]	Reference
σ_0	497	1195 – 1533	A2MAMI-2019 [54]
	969	1300 – 1900	A2MAMI-2018 [55]
	497	1204 – 1869	Ref. [56]
Σ	216	1484 – 1912	GRAAL-2009 [57]
<i>E</i>	154	1312 – 1888	A2MAMI-2017 [58]

FIG. 5: Experimental data for $\pi^0 n$ channel. Notations as in Fig. 2. Black points correspond to the Ref. [56].

[59]. The statistical uncertainties are so small, that systematic uncertainties due to angular dependent detection efficiencies had to be taken into account. For all other observables the uncertainties in the angular distributions are dominated by statistics. Normalization errors (luminosity, polarization degree) are below of 5% and are not taken into account in this analysis. For our single-energy fits we need all observables at the same values of $W = \sqrt{s}$ and for the fixed- t fits at the same values of t . Typically this is not provided by the experiments directly. The data are given in bins of W and center of mass angle θ_{cm} with bin sizes and central values varying between different data sets. Therefore some interpolation between measurements at different energies and angles is necessary. We have used a spline smoothing method [60] which was similarly applied in the Karlsruhe-Helsinki analysis KH80 [13] and in our previous analysis of η production [10]. The uncertainties of interpolated data points are taken to be equal to the errors of nearest measured data points. Our fixed- t amplitude analysis is performed at 43 t -values in the range $-1.00 \text{ GeV}^2 < t < -0.005 \text{ GeV}^2$. Examples of interpolated data points are shown in Figs. 6 and 7.

B. Fixed- t amplitude analysis

As starting solutions in our iterative procedure we use three different energy dependent analyses, which can provide a full set of three isospin amplitudes for both, proton and neutron channels, SE1: BnGa2019 (Bonn-Gatchina group) [1], SE2: SAID-M19 (GWU-SAID group) [61] and SE3: MAID2007 (MAID group) [4]. Each invariant amplitude is fitted with 30 parameters in Pietarinen’s expansion.

Our iterative procedure, graphically described in Fig. 1, converges very quickly after typically 3 iterations. In the following we only show the final solutions after convergence has been reached. Further details about the iterative procedure can be found in our earlier PWA for η photoproduction, Ref. [10].

Although our three starting solutions can be very different in some kinematical regions, all of them lead to good fits to the data with practically the same χ^2 values.

Eventhough our three different starting solutions converge to three solutions that are much closer together, we also create an “averaged” solution SEav by performing an average over our three SE solutions and taking this solution as input for the first iteration in the final fitting procedure. Figs. 6 and 7 show the final fit to the data at fixed t , using as starting solution the “averaged” solution.

1. Fixed- t experimental data and Pietarinen fits

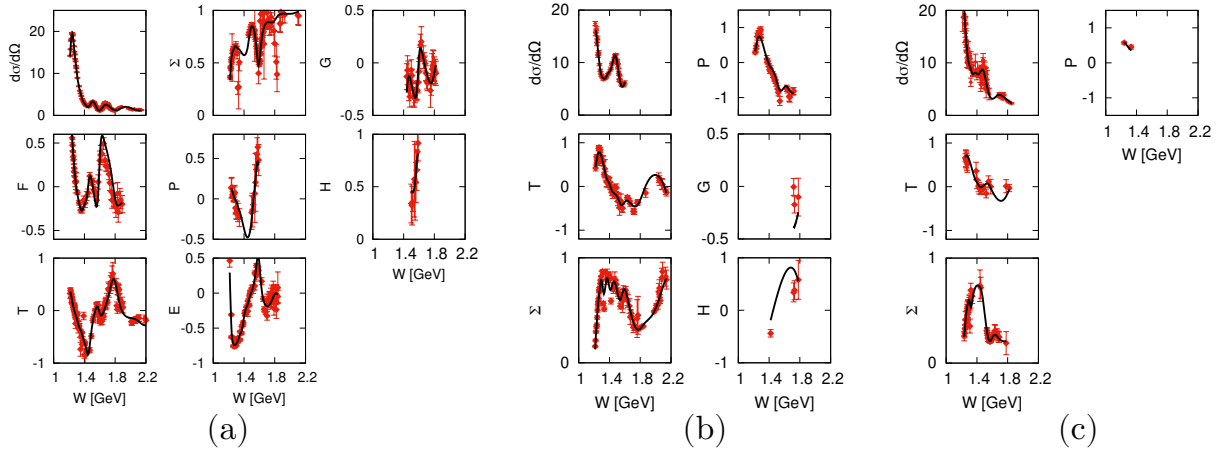


FIG. 6: Fixed- t fits at $t = -0.2 \text{ GeV}^2$ for reactions (a) $p(\gamma, \pi^0)p$, (b) $p(\gamma, \pi^+)n$ and (c) $n(\gamma, \pi^-)p$. Solid lines show the final solutions after convergence in the iterative procedure.

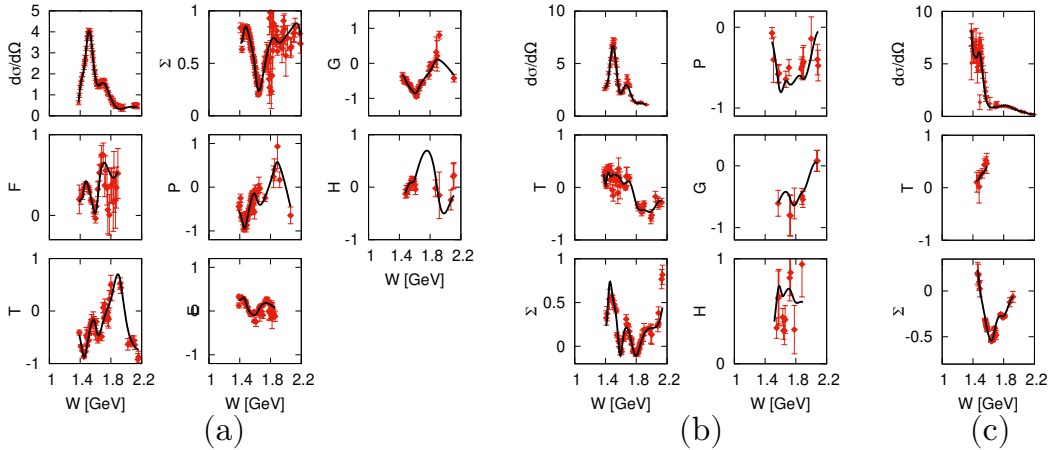


FIG. 7: Fixed- t fits at $t = -0.5 \text{ GeV}^2$ for reactions (a) $p(\gamma, \pi^0)p$, (b) $p(\gamma, \pi^+)n$ and (c) $n(\gamma, \pi^-)p$. Solid lines show the final solutions after convergence in the iterative procedure.

2. Fixed- t helicity amplitudes

In our iterative procedure (see Fig. 1) we use helicity amplitudes as constraints. For the fixed- t fits these are helicity amplitudes obtained in the previous SE fit at fixed W , while for the single-energy fits we need helicity amplitudes obtained in the previous fixed- t fit.

Figs. 8, 9 show real and imaginary parts of the helicity amplitudes at fixed t as functions of W after convergence has been reached in our iterative procedure. The blue and red dots are the real and imaginary parts, obtained from the final SE fits. Full lines are the helicity amplitudes from final iteration in fixed- t AA. (For these final solutions we used the averaged solution as the starting solution.)

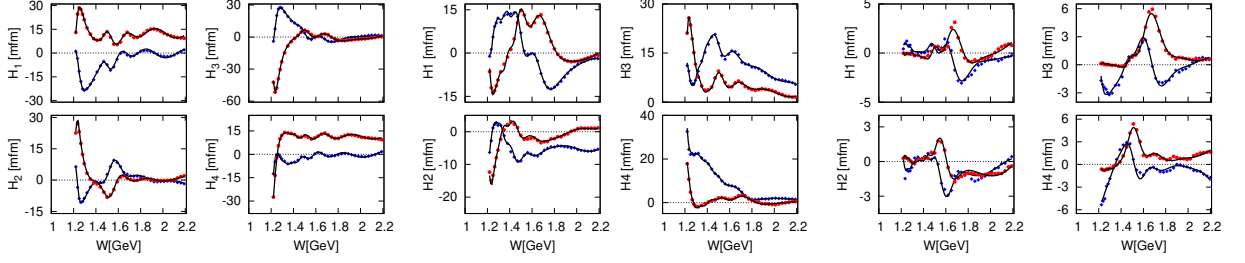


FIG. 8: Helicity amplitudes at $t = -0.2 \text{ GeV}^2$ for isospin combinations $(+, -, 0)$, respectively. The blue and red points show real and imaginary parts of the final PWA SE solution, and the solid lines are obtained in the final FT AA.

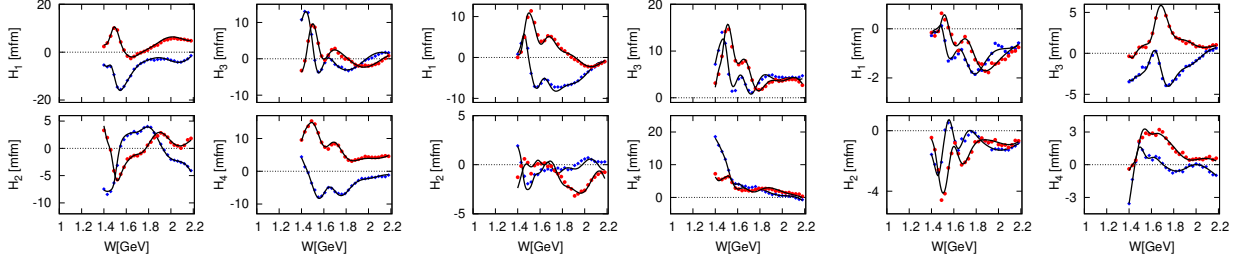


FIG. 9: Helicity amplitudes at $t = -0.5 \text{ GeV}^2$ for isospin combinations $(+, -, 0)$, respectively. The blue and red points show real and imaginary parts of the final PWA SE solution, and the solid lines are obtained in the final FT AA.

C. Constrained single-energy PWA

In the single-energy partial wave analysis we consider 135 energy bins in the range $1.09 \text{ GeV} < W < 2.2 \text{ GeV}$. The obtained electric and magnetic multipoles were finally binned in 45 energy bins.

1. SE experimental data and PWA fits

Figures 11 - 14 show the final fits to the experimental data and predictions for other unmeasured observables at four different energies, $W = (1210, 1420, 1630, 1840) \text{ MeV}$. The observables are presented in four rows for the charged channels, $p(\gamma, \pi^0)p$, $p(\gamma, \pi^+)n$, $n(\gamma, \pi^-)p$ and $n(\gamma, \pi^0)n$, from top to bottom. Most observables (up to seven) and best statistics is provided by the $p(\gamma, \pi^0)p$ data, but also the $p(\gamma, \pi^+)n$ data have mostly good statistics and could be used with up to six observables. The $n(\gamma, \pi^-)p$ has also good statistics, and could be used with up to four observables. Finally, the neutral channel, $n(\gamma, \pi^0)n$, which has not been used in our fits, appears in up to three observables, $d\sigma/d\Omega, \Sigma, E$. Even as newer data also appear with quite good statistics, due to the difficult separation from the nuclear γ, π^0 reaction, their systematical errors can be much larger and are still under discussion.

Our fits (red solid lines) describe the used data in the first three channels very well, see also Fig. 10 with the χ^2/N_{data} values. The data in the neutral channel are only reasonably described. A real discrepancy in this channel would be a violation of isospin symmetry. However, unknown systematical errors, as mentioned before, are much more likely.

Besides the final solution (red lines), we also show the three solutions, SE1, SE2, SE3, obtained with the starting solutions of BnGa2019, SAID-M19, MAID2007, as black, blue and green lines. For all fitted observables all four solutions coincide and have the same χ^2 values, see Fig. 10.

Comparing these four solutions for unmeasured observables gives an interesting insight into the problem of complete experiments. Starting at the lowest energy, $W = 1210 \text{ MeV}$ (Fig. 11), the four solutions fully agree in almost all cases, telling that the experiment with only five observables for π^0p , two for π^+n and π^-p is practically complete.

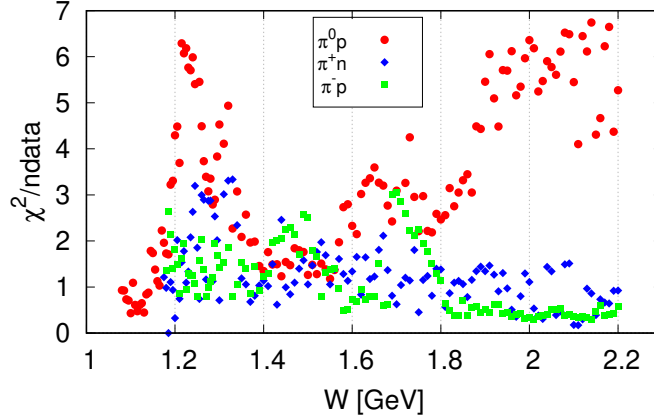


FIG. 10: χ^2 values per data points for the three fitted reaction channels, $p(\gamma, \pi^0)p$ (red), $p(\gamma, \pi^+)n$ (blue) and $n(\gamma, \pi^-)p$ (green). The fits were performed in 135 energy bins, the obtained electric and magnetic multipoles were binned in 45 energy bins.

Visible ambiguities are only present for P, G, H of $\pi^0 n$ in the bottom row. The reason for this very positive result is certainly the very high statistics of the data, but also the unitarity constraint, Watson's theorem.

The situation changes a little bit, when moving forward to the next selected energy, $W = 1420$ MeV (Fig. 12). This energy is nominally above the $\pi\pi$ threshold, however, as it is known for a long time, the Watson theorem only breaks down with the onset of the next inelastic nucleon resonances. And these are $N(1440)1/2^+$, $N(1520)3/2^-$, $N(1535)1/2^-$ in the second resonance region. For this energy we can compare older and new data on the neutral $n(\gamma, \pi^0)n$ reaction (d). While the new data [55] has very high statistics, it does not overlap with the older data [56] even with much larger statistical errors. Our analysis, which does not need these neutral channel data, supports the older data.

Going above these energy limits, Figs. 13 and 14 show the observables at $W = 1630$ MeV and $W = 1840$ MeV. While the fitted observables still completely overlap, the predictions move apart for our four solutions, showing clear ambiguities, most pronounced in the two neutron channels. In the proton channels, for π^0 the solutions are still rather unique, but already in the π^+ channel strong deviations appear and become stronger with energy. The reason is manifold, no Watson constraint, no constraint anymore from Born terms and larger number of partial waves are contributing. Here, the available polarization observables clearly do not form anymore a complete or almost complete experiment. But with additional polarization observables, even without recoil polarization, unique solutions could be obtained [8].

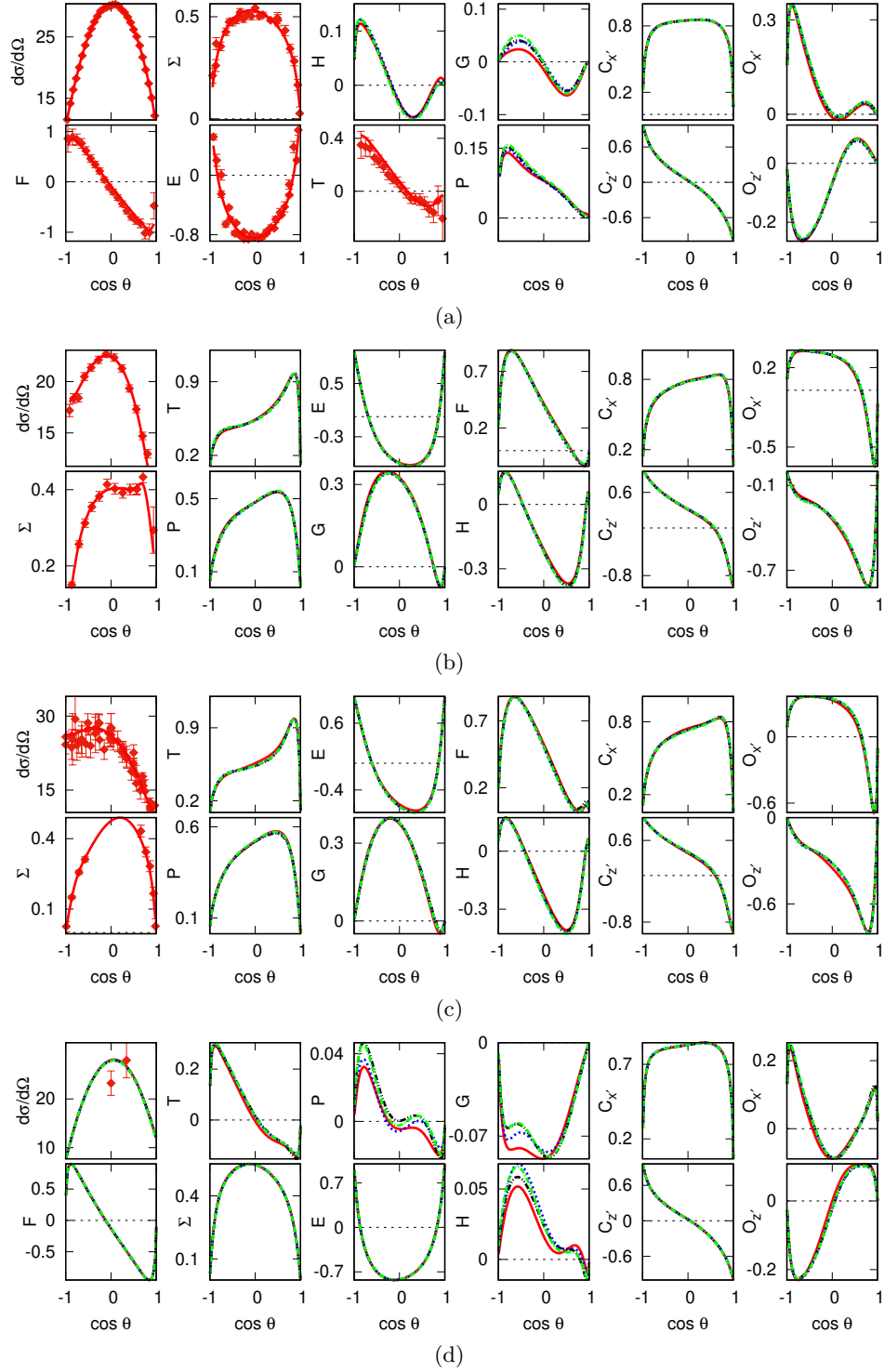


FIG. 11: Single-energy fit to the experimental data and predictions for polarization observables that are not fitted at $W = 1210$ MeV. Predictions from four different single-energy solutions, SE1 (black dot-dot-dashed line), SE2 (blue short-dashed line), SE3 (green dashed-dotted line) and SEav (solid red line) for polarization observables that are not fitted. In (a), (b) and (c) single-energy fits SEav are shown and compared to the experimental data (red dots) for $p(\gamma, \pi^0)p$, $p(\gamma, \pi^+)n$ and $n(\gamma, \pi^-)p$ reactions, and predictions for polarization observables, respectively. In (d) predictions for polarization observables are shown, that are not experimentally measured for the reaction $n(\gamma, \pi^0)n$. Experimental data for $n(\gamma, \pi^0)n$ reaction are not fitted in our isospin analysis.

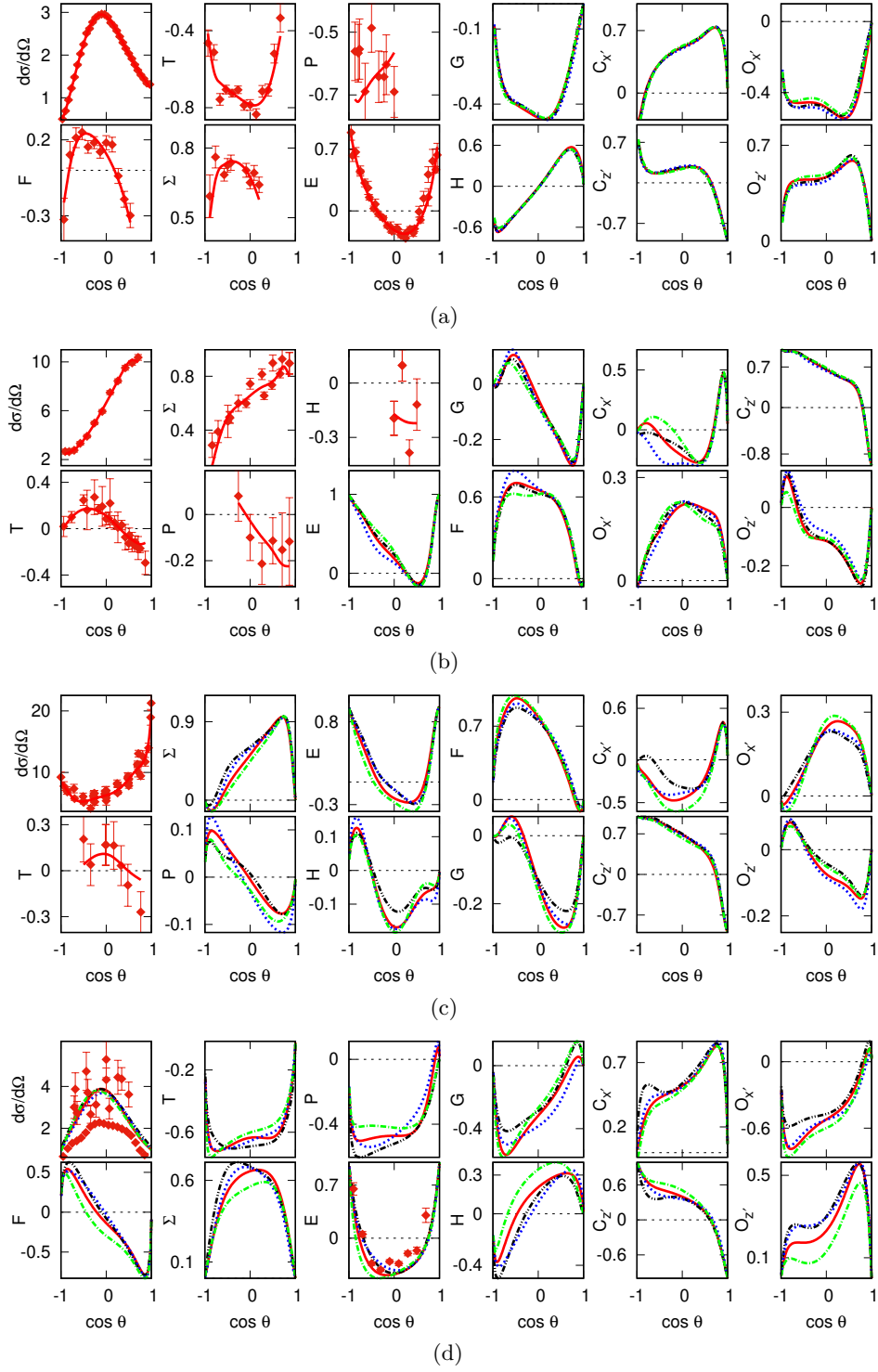


FIG. 12: Single-energy fit to the experimental data and predictions for polarization observables that are not fitted at $W = 1420$ MeV. The new data with high statistics for the neutral channel (d) are from Ref.[55]. Notations as in Fig. 11.

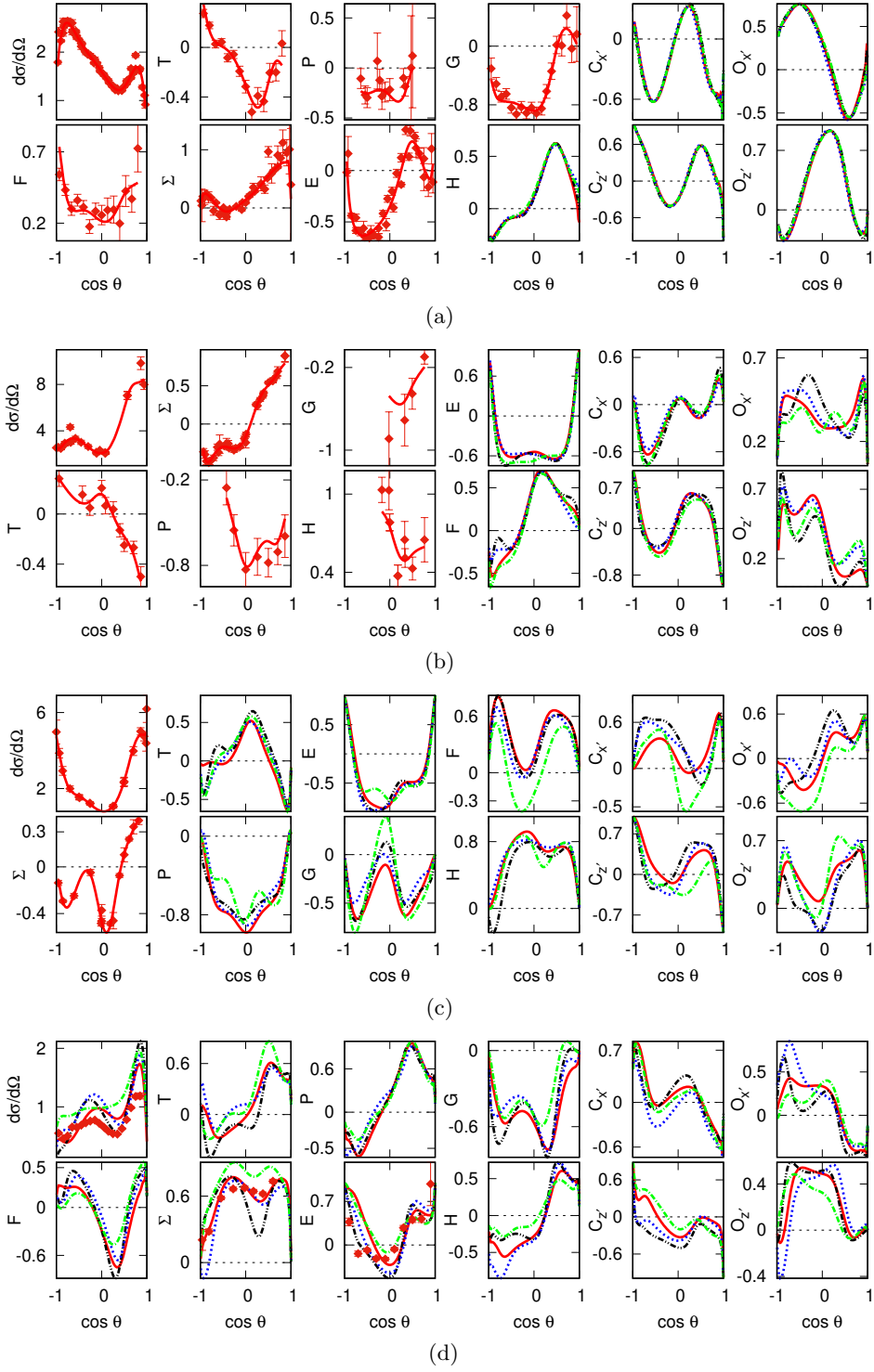


FIG. 13: Single-energy fit to the experimental data and predictions for polarization observables that are not fitted at $W = 1630$ MeV. Notations as in Fig. 11.

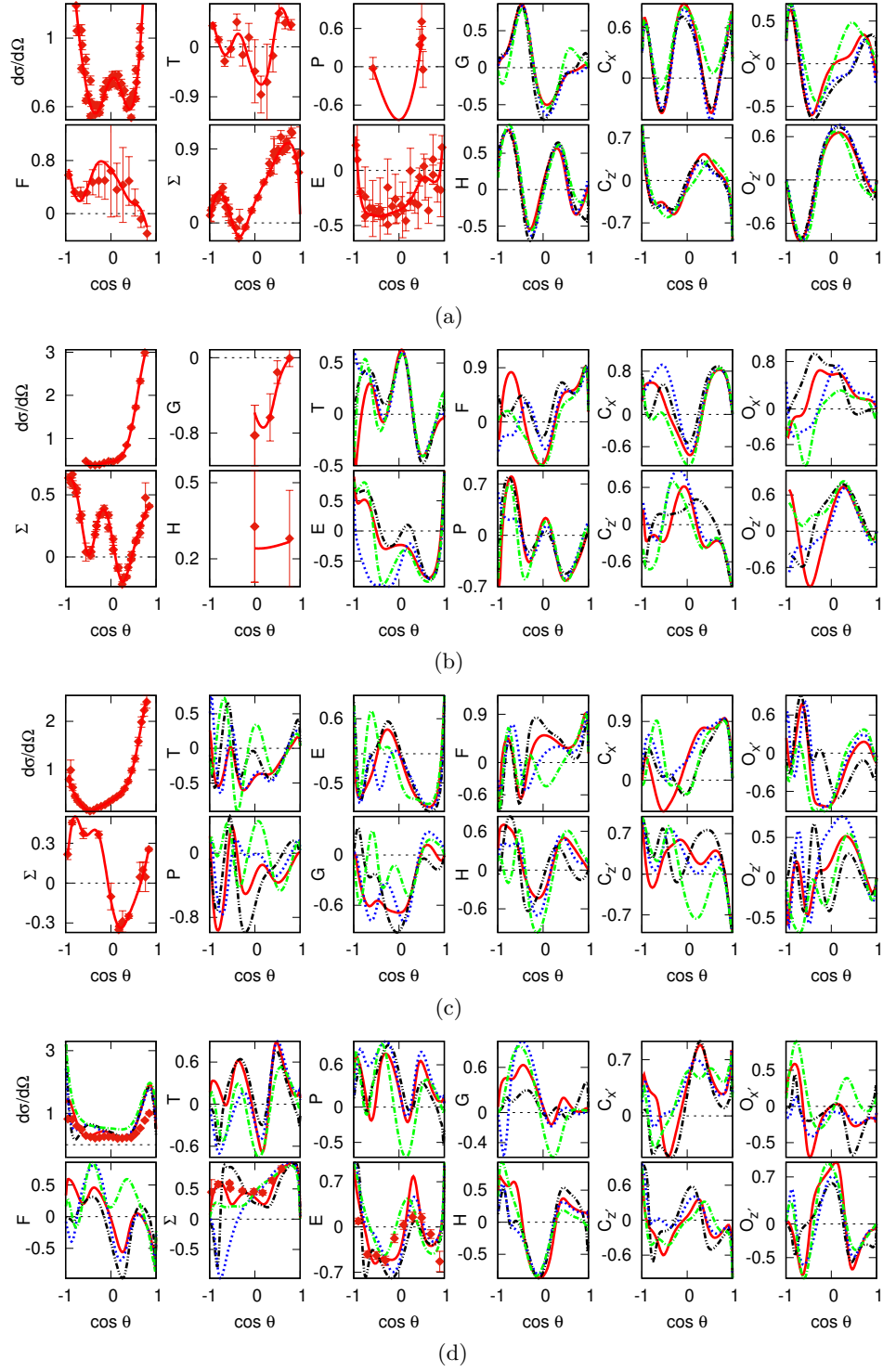


FIG. 14: Single-energy fit to the experimental data and predictions for polarization observables that are not fitted at $W = 1840$ MeV. Notations as in Fig. 11.

2. Helicity amplitudes from SE PWA

Figure 15 shows the helicity amplitudes $H_i(W, \theta), i = 1, \dots, 4$ that are used as the fixed- t constraint in the single-energy partial wave analysis of step 2, see Eqs. (3, 4). The figures show the final situation after convergence has been reached in the iterative procedure. The blue and red points are the real and imaginary parts of the amplitudes from the (previous) FT AA and exhibit a mild statistical fluctuation as each θ value stems from a different fixed- t analysis. At the highest energies the kinematical limitation becomes visible, as we reach the kinematical limit with our smallest t -value of -1.00 GeV^2 already around 90° , see the Mandelstam diagram in appendix A. The final SE PWA results with reconstructed helicity amplitudes from partial waves are shown as solid lines and completely overlap the blue and red points, demonstrating the perfect convergence of the iteration.

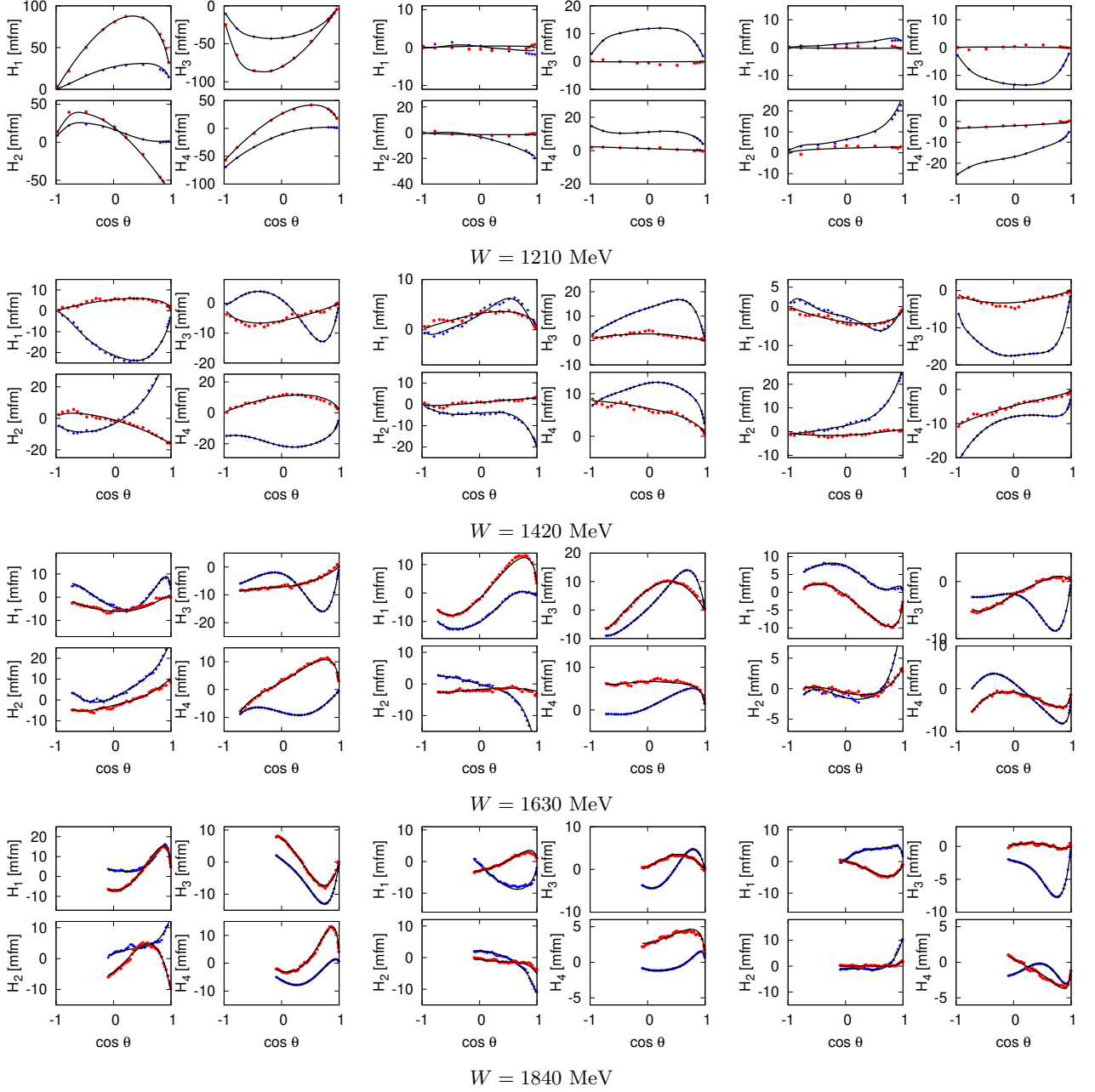


FIG. 15: Real and imaginary parts of the helicity amplitudes (blue and red dots) from individual fixed- t AA at different t -values in the final iteration. Full lines are the helicity amplitudes from final iteration in SE PWA. Three columns show results for isospin 3/2, and isospin 1/2 with proton and neutron targets, respectively. From top to bottom, the fixed energy values are $W = (1210, 1420, 1630, 1840) \text{ MeV}$ and correspond to the previous figures 11 - 14

D. Multipoles

The final result of our partial wave analysis are the electric and magnetic multipoles $E_{\ell\pm}, M_{\ell\pm}$ at discrete energy values W . For better convergence we have performed our PWA up to $\ell_{max} = 5$, but discuss the multipoles only up to F waves ($\ell = 3$). Higher partial waves are dominated by various background contributions, while nucleon resonances with ($\ell > 3$) show up at larger energies beyond our investigated region. In full isospin formalism, the multipoles as well as also other amplitudes can be given in different representations, depending on the physics issues that are being discussed. Typically, nucleon resonances have definite isospin and, therefore, partial waves are best discussed in representations with good isospin. However, when non-resonant effects as final-state interactions and chiral loop effects at low energies or Regge models at high energies are discussed, other representations are more helpful. For example, the MAID program [4] allows to study four different representations, definitions and relations between them are given in appendix D. In this section we show figures in three different representations: Figs. 16 - 21 show amplitudes with isospin 3/2 and isospin 1/2 with proton and neutron targets, $A^{(3/2)}, A_p^{(1/2)}$ and $A_n^{(1/2)}$, Figs. 22 - 24 show isovector $A^{(+)}, A^{(-)}$, which are mixtures of isospin 1/2 and 3/2, and isoscalar $A^{(0)}$ amplitudes with isospin 1/2. Finally, Figs. 25 - 28 show the amplitudes in the four different charge channels, which are closer connected to the measured observables.

First, we will discuss the isospin amplitudes, which are the basic results of our fitting procedure, while the other representations are simply obtained by linear transformations.

1. Isospin multipoles from different initial solutions

Figs. 16 - 18 show intermediate results, where our three SE1, SE2 and SE3 solutions, that started with BnGa2019, SAID-M19 and MAID2007, are compared. At low energies the different and independent solutions are very similar and coincide very well inside their statistical errors. This is consistent with our observation, when we discussed the SE fits of the observables in Figs. 11 - 14. In the energy region from threshold up to $W \approx 1400$ MeV, the experiments are already almost complete and the partial wave solutions appear practically free of ambiguities.

At higher energies, still some partial waves, especially M_{1+} in the P_{33} channel, show only very mild variations. But the bulk part of partial waves appear with larger spreads and larger statistical uncertainties at energies $W > 1600$ MeV.

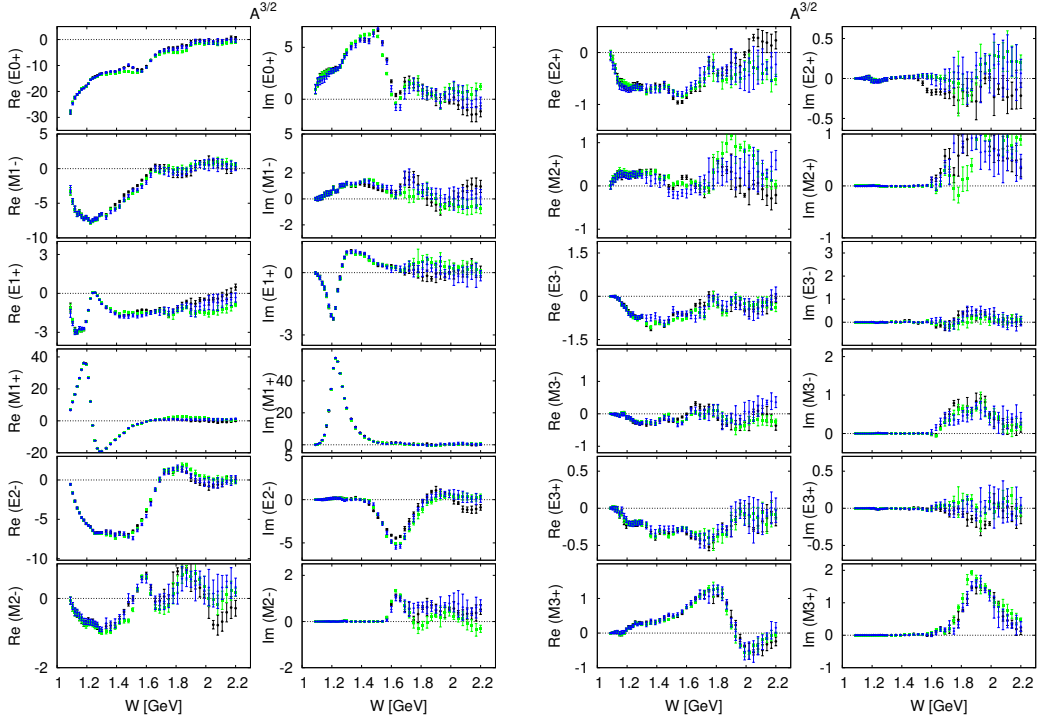


FIG. 16: Electric and magnetic multipoles for isospin 3/2 are shown from three different analyses, SE1 (black), SE2 (blue), SE3 (green), using as initial solutions BnGa2019, SAID-M19 and Maid2007, respectively. Multipoles are given in units of am ($am \equiv mfm$).

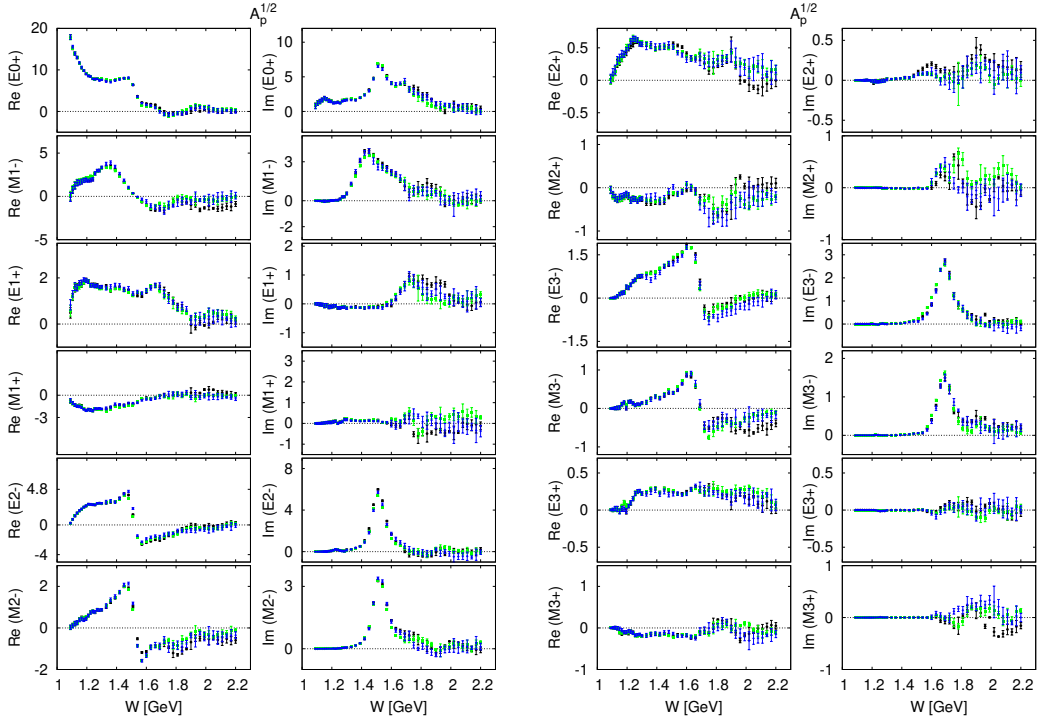


FIG. 17: Electric and magnetic multipoles for isospin 1/2 with a proton target are shown from three different analyses, SE1 (black), SE2 (blue), SE3 (green), using as initial solutions BnGa2019, SAID-M19 and Maid2007, respectively. Multipoles are given in units of am ($am \equiv mfm$).

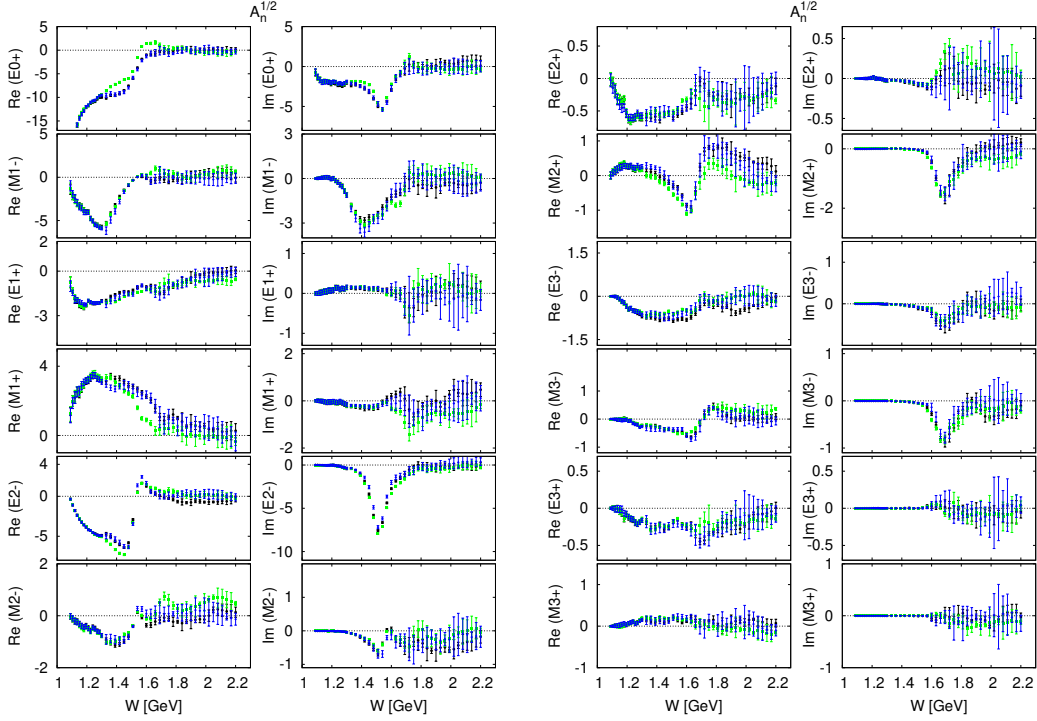


FIG. 18: Electric and magnetic multipoles for isospin 1/2 with a neutron target are shown from three different analyses, SE1 (black), SE2 (blue), SE3 (green), using as initial solutions BnGa2019, SAID-M19 and Maid2007, respectively. Multipoles are given in units of am ($am \equiv mfm$).

2. Isospin multipoles from averaged solution and comparison with models

In Figs. 19 - 21 our final results (SEav) are shown and compared to present ED solutions from BnGa, GWU-SAID and MAID. From a global view, these figures give a consistent picture of the partial waves. In most partial waves and most energy regions the ED solutions appear within the statistical uncertainties of our SEav solution. Looking into the details, nevertheless some remarks should be done. For some multipoles, as $E_{0+}^{(3/2)}$, $E_{2-}^{(3/2)}$, $E_{3-}^{(3/2)}$, MAID2007 (green, dash-dotted), differs significantly from our new solution. This is not a surprise, as first of all, MAID2007 is the oldest solution compared here, and furthermore, it was only fitted up to $W = 1.7$ GeV. In fact this also explains, while this rather old PWA is still often used, especially as it also provides extensions into the virtual photon region.

But also the newer BnGa2019 (black, dot-dot-dashed) and new SAID-M19 (blue, dotted) solutions differ significantly for some multipoles. E.g. BnGa solution differs mostly in $\text{Im } E_{2+}^{(3/2)}$, $\text{Im } pM_{1+}^{(1/2)}$ and $\text{Im } nM_{1+}^{(1/2)}$, whereas the SAID-M19 (newest) solution compares best with our SE solution.

Furthermore, it is worth to note, that our new SE solution exhibits local structures in some multipoles, which are not present in either of those ED solutions. These are visible in $\text{Im } M_{1-}^{(3/2)}$ and $M_{2+}^{(3/2)}$. In a forthcoming nucleon resonance analysis with e.g. the L+P formalism, it can be investigated whether this structure gives new insights in the nucleon resonance content.

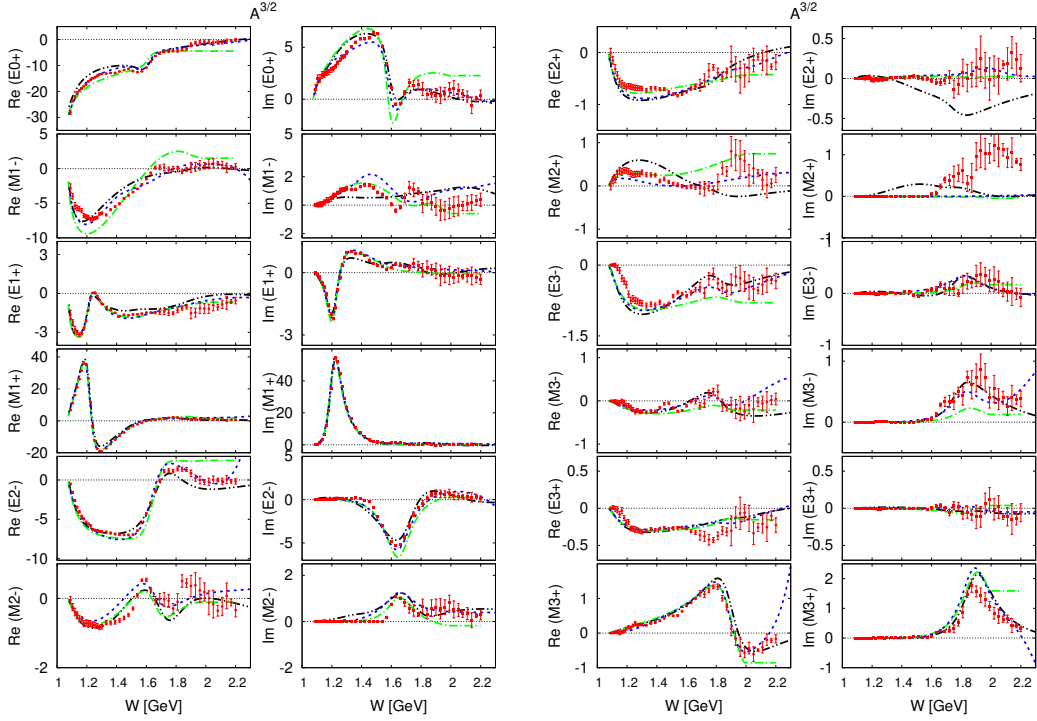


FIG. 19: Electric and magnetic S, P, D, F multipoles for isospin $3/2$, $A^{(3/2)}$. The data points show the final SEav solution, using the averaged starting solution in the iterative procedure. The black (dot-dot-dashed), blue (dotted) and green (dash-dotted) lines are ED solutions from BnGa2019, SAID-M19 and Maid2007, respectively. Multipoles are given in units of am ($am \equiv \text{mfm}$).

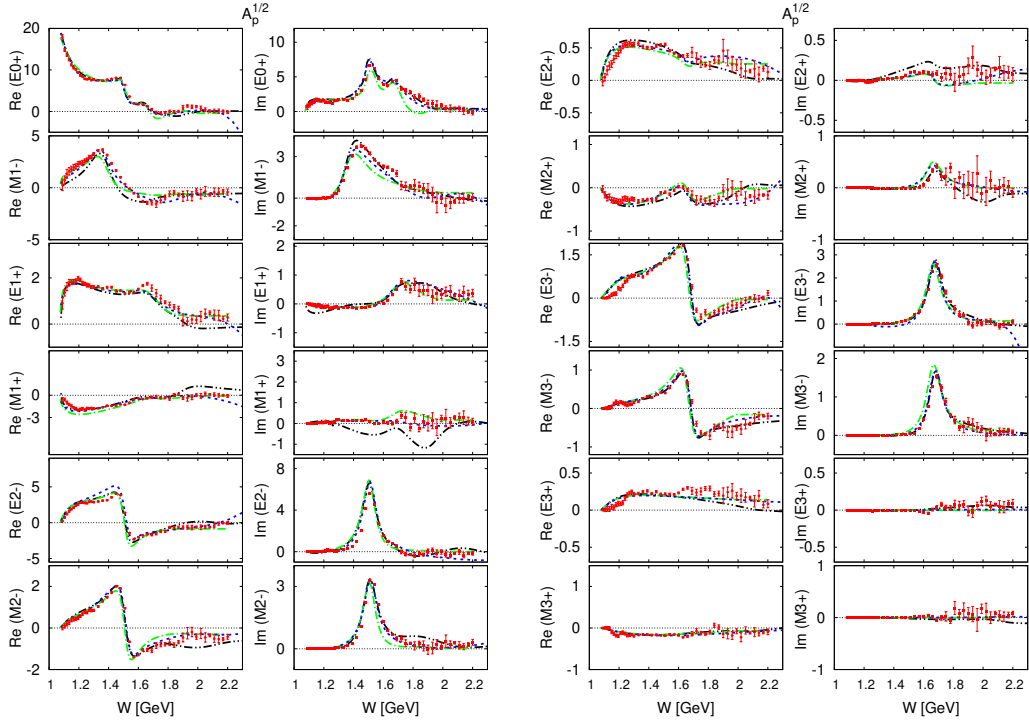


FIG. 20: Electric and magnetic S, P, D, F multipoles for isospin $1/2$ with a proton target, $A_p^{(1/2)}$. Notation as in Fig. 19

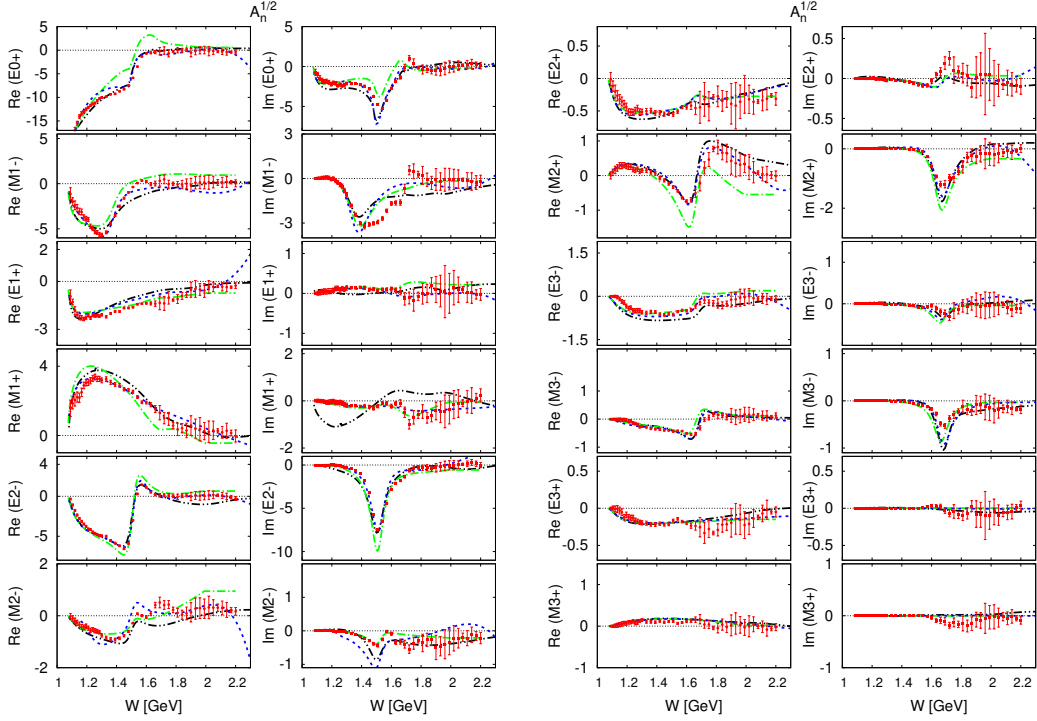


FIG. 21: Electric and magnetic S, P, D, F multipoles for isospin 1/2 with a neutron target, $A_n^{(1/2)}$. Notation as in Fig. 19

3. Isovector and isoscalar multipoles (+, -, 0).

Next we calculated the isospin combinations (+, -, 0) for isovector and isoscalar multipoles from the fitted isospin amplitudes ($A^{(3/2)}, A_p^{(1/2)}, A_n^{(1/2)}$) and make comparison with the ED solutions of MAID2007 (green, dash-dotted), BnGa2019 (black, dot-dot-dashed) and SAID-M19 (blue, dotted). In this representation the old MAID2007 solution competes even better with the newer ones. A remarkable result can be observed in the isovector S -wave amplitude $E_{0+}^{(+)}$ between pion and eta threshold. There, the newest SAID-M19 PWA agrees well with our SE analysis, whereas both BnGa2019 and MAID2007 differ substantially, but in quite different ways.

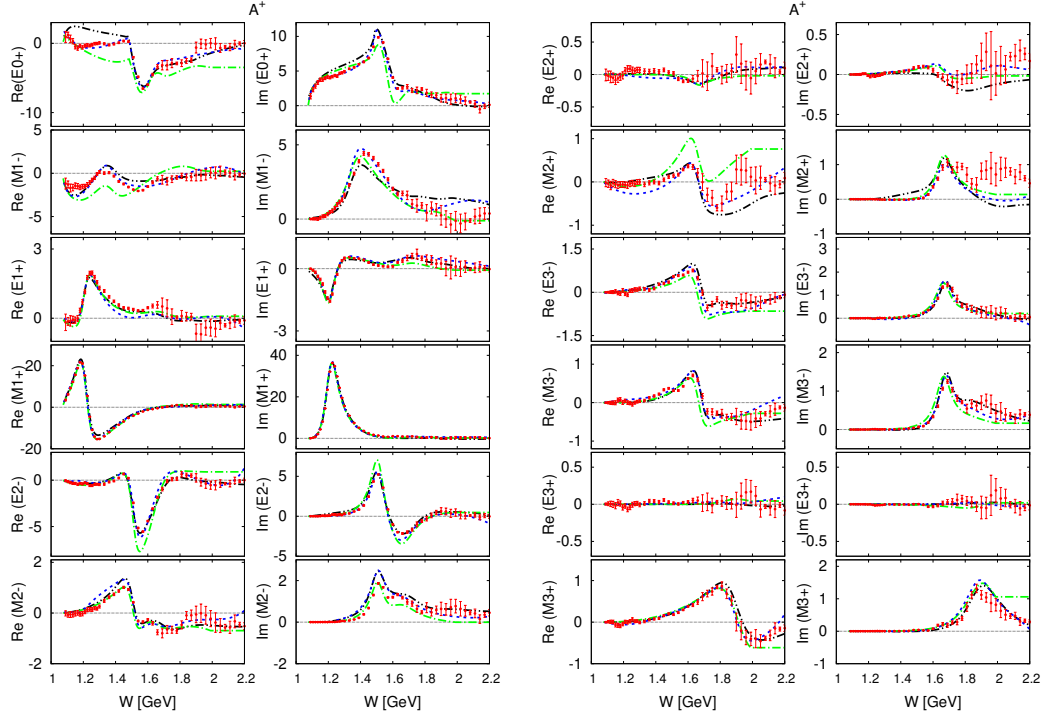


FIG. 22: Electric and magnetic S, P, D, F isovector multipoles $A^{(+)}$, see definition Eq. (D5), appendix D. Notation as in Fig. 19.

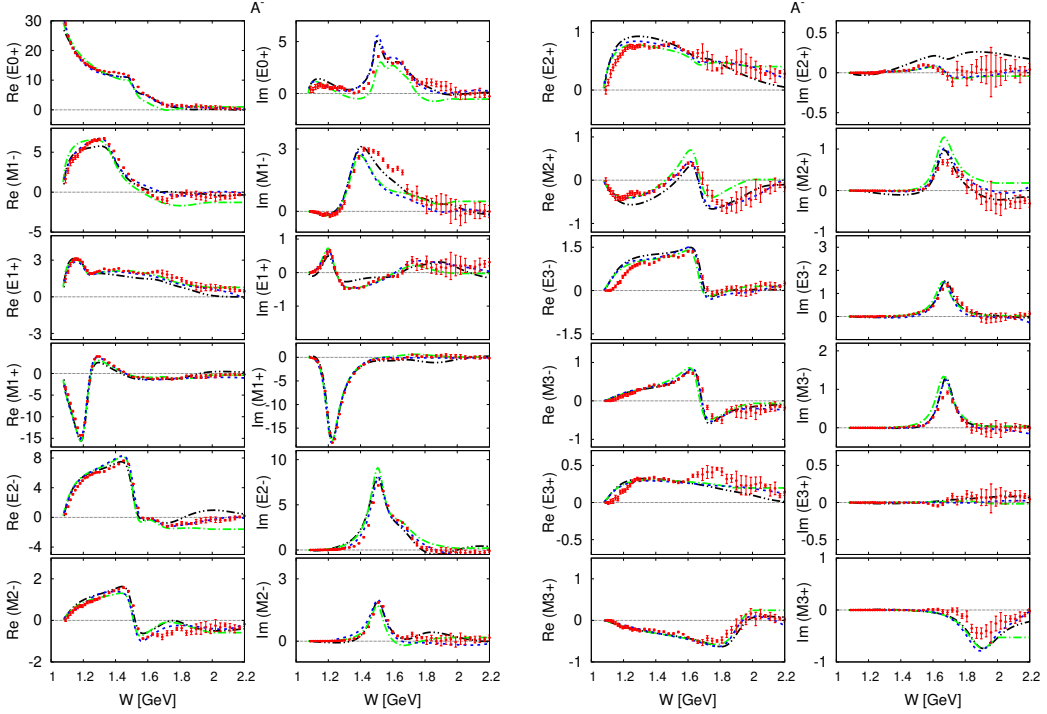


FIG. 23: Electric and magnetic S, P, D, F isovector multipoles $A^{(-)}$, see definition Eq. (D6), appendix D. Notation as in Fig. 19.

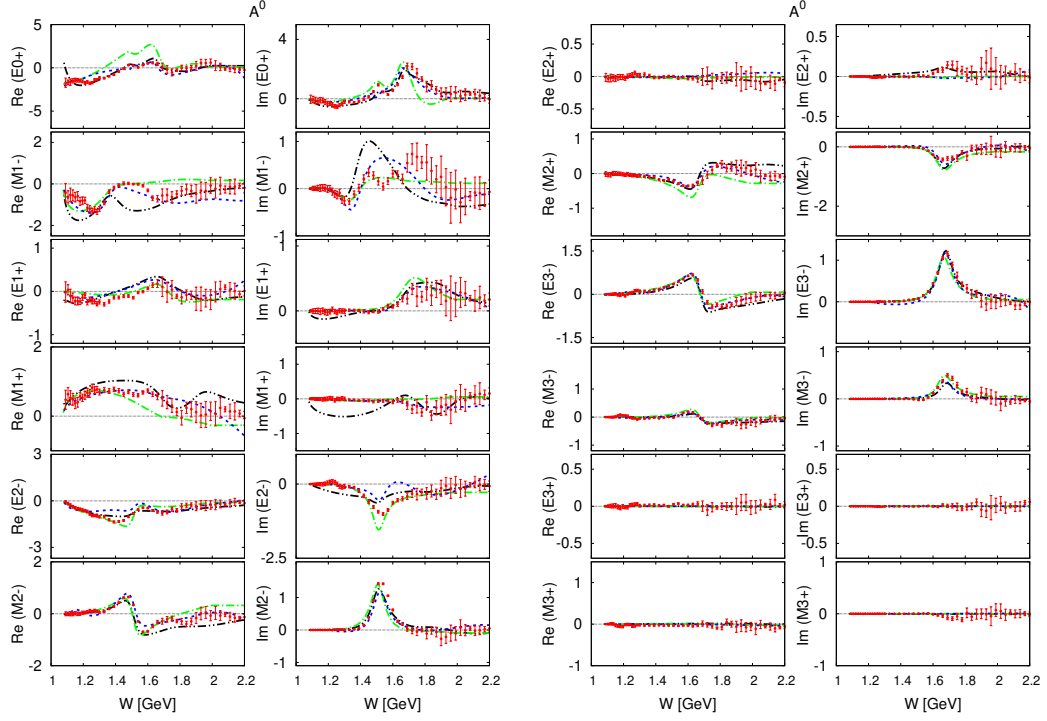


FIG. 24: Electric and magnetic S, P, D, F isoscalar multipoles $A^{(0)}$, see definition Eq. (D7), appendix D. Notation as in Fig. 19.

4. Multipoles for charged channels

For completeness we also recalculated the multipoles for the four charged channels from the fitted isospin amplitudes ($A^{(3/2)}$, $A_p^{(1/2)}$, $A_n^{(1/2)}$) and compared with the three ED solutions, which were used as starting solutions for the iterative procedure, see Figs. 25 - 28.

In this charge separation, the S -wave multipole for $p(\gamma, \pi^0)p$ exhibits a strong deviation at low energies between the pion and eta thresholds. The effect which was already visible in the isovector (+) representation becomes more pronounced.

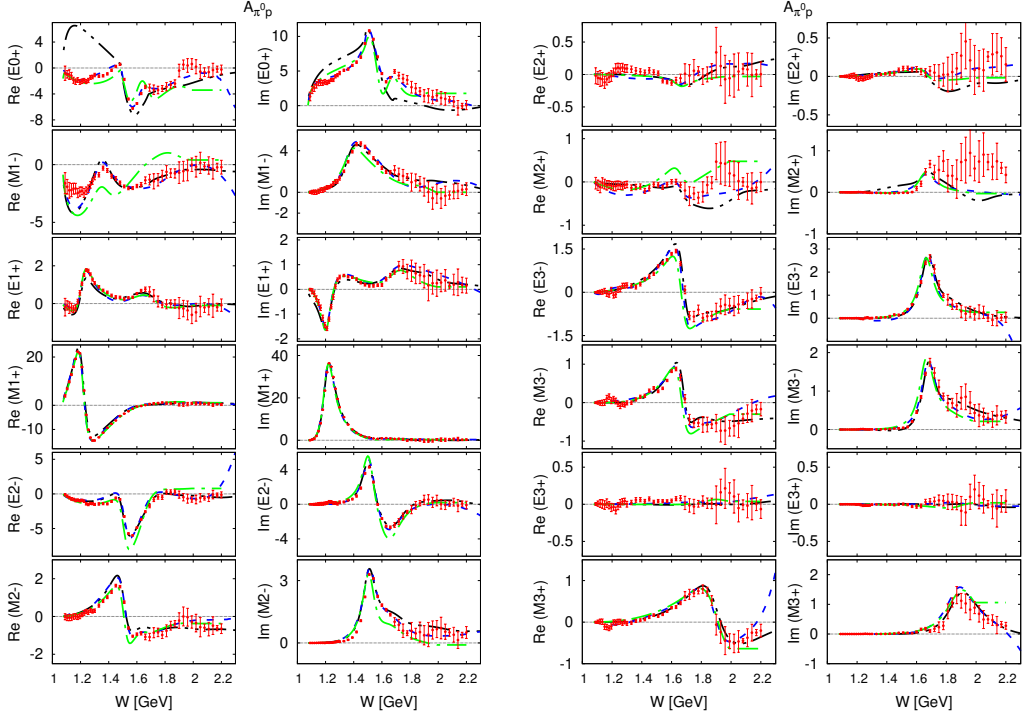


FIG. 25: Electric and magnetic S, P, D, F waves for reaction $p(\gamma, \pi^0)p$, see definition Eq. (D1), appendix D. Notation as in Fig. 19.

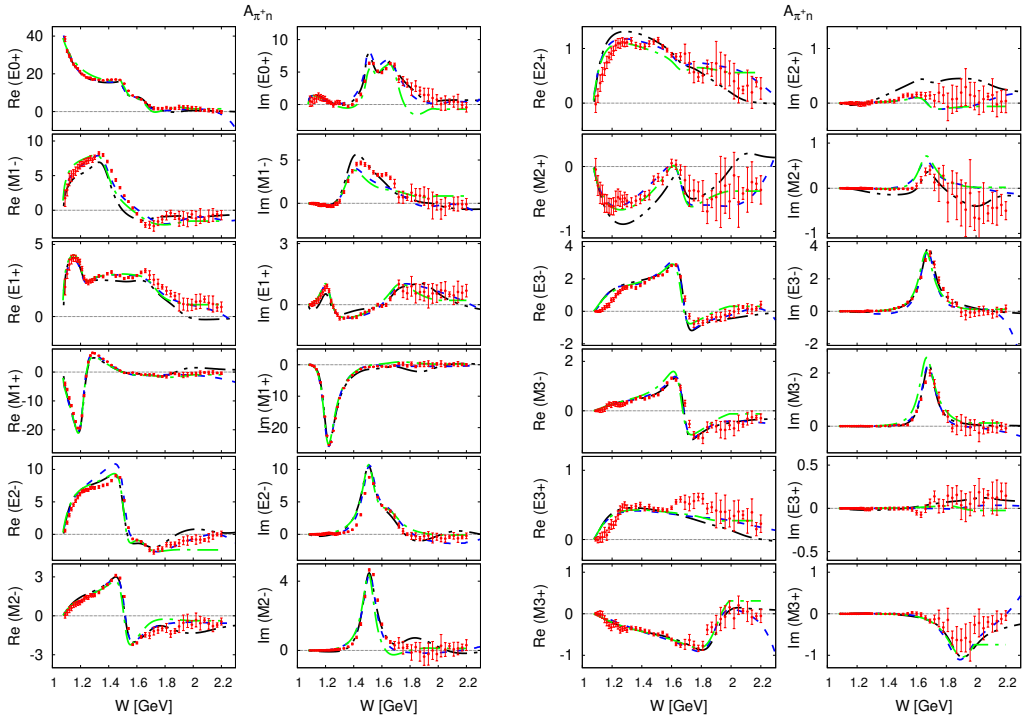


FIG. 26: Electric and magnetic S, P, D, F waves for reaction $p(\gamma, \pi^+)n$, see definition Eq. (D1), appendix D. Notation as in Fig. 19.

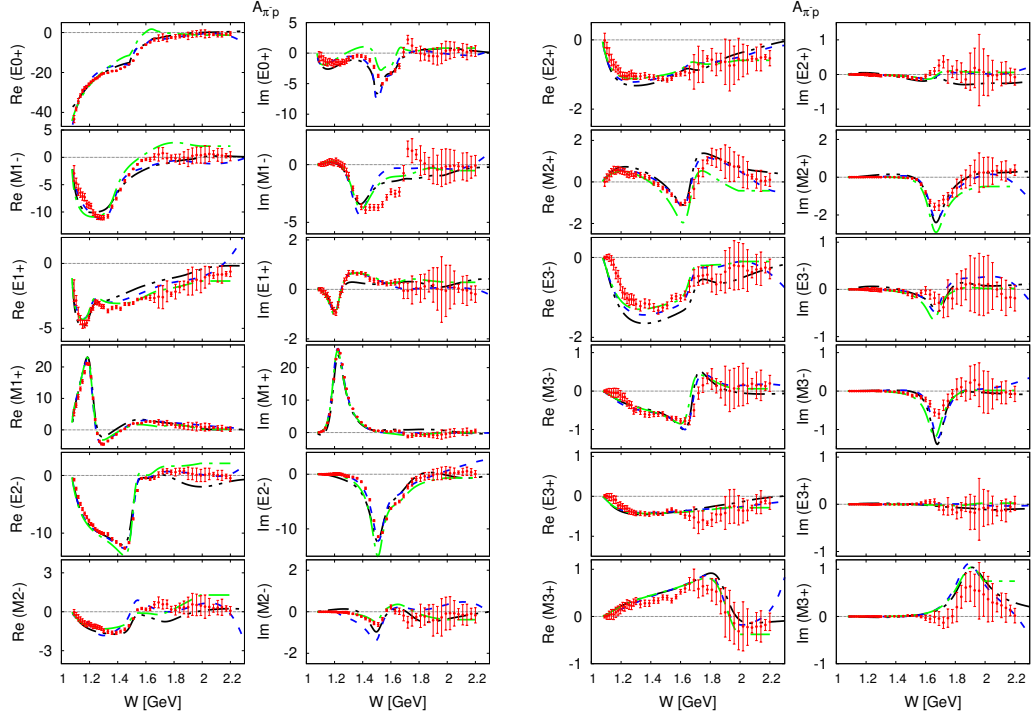


FIG. 27: Electric and magnetic S, P, D, F waves for reaction $n(\gamma, \pi^-)p$, see definition Eq. (D1), appendix D. Notation as in Fig. 19.

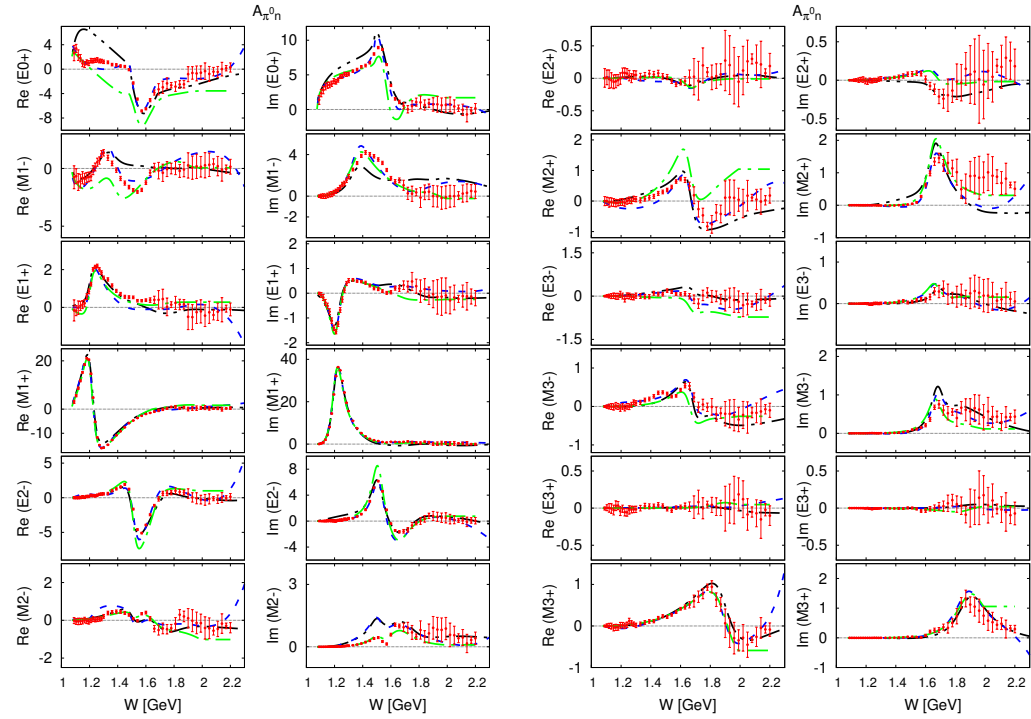


FIG. 28: Electric and magnetic S, P, D, F waves for reaction $n(\gamma, \pi^0)n$, see definition Eq. (D1), appendix D. Notation as in Fig. 19.

E. Phases

Finally, in Fig. 29 we compare the phases of our photoproduction multipoles from the final solution SEav with the pion-nucleon phases from phase-shift analyses of Karlsruhe 1984 [62] and GWU/SAID 2006 [63]. From 2-body unitarity the Watson theorem follows, stating, that below two-pion production threshold, the phases of pion photoproduction multipoles must be the same as the pion-nucleon phases of the same final states. As we have included the unitarity as a constraint in our PWA, the Watson theorem is perfectly fulfilled as can be seen in the figure for energies up to $W \approx 1400$ MeV. This energy is already about 150 MeV above the two-pion threshold, but since the opening of inelastic channels for $\gamma N \rightarrow \pi\pi N$ is rather weak in this energy region, no deviation in the phases is visible. Even above this energy, many partial waves remain practically elastic even up to $W \approx 1600$ MeV. Certainly, due to strong inelastic contributions from $N(1440)1/2^+$, $N(1520)3/2^-$, $N(1535)1/2^-$ resonances, the P_{11}, D_{13}, S_{11} multipoles deviate from the πN phases first.

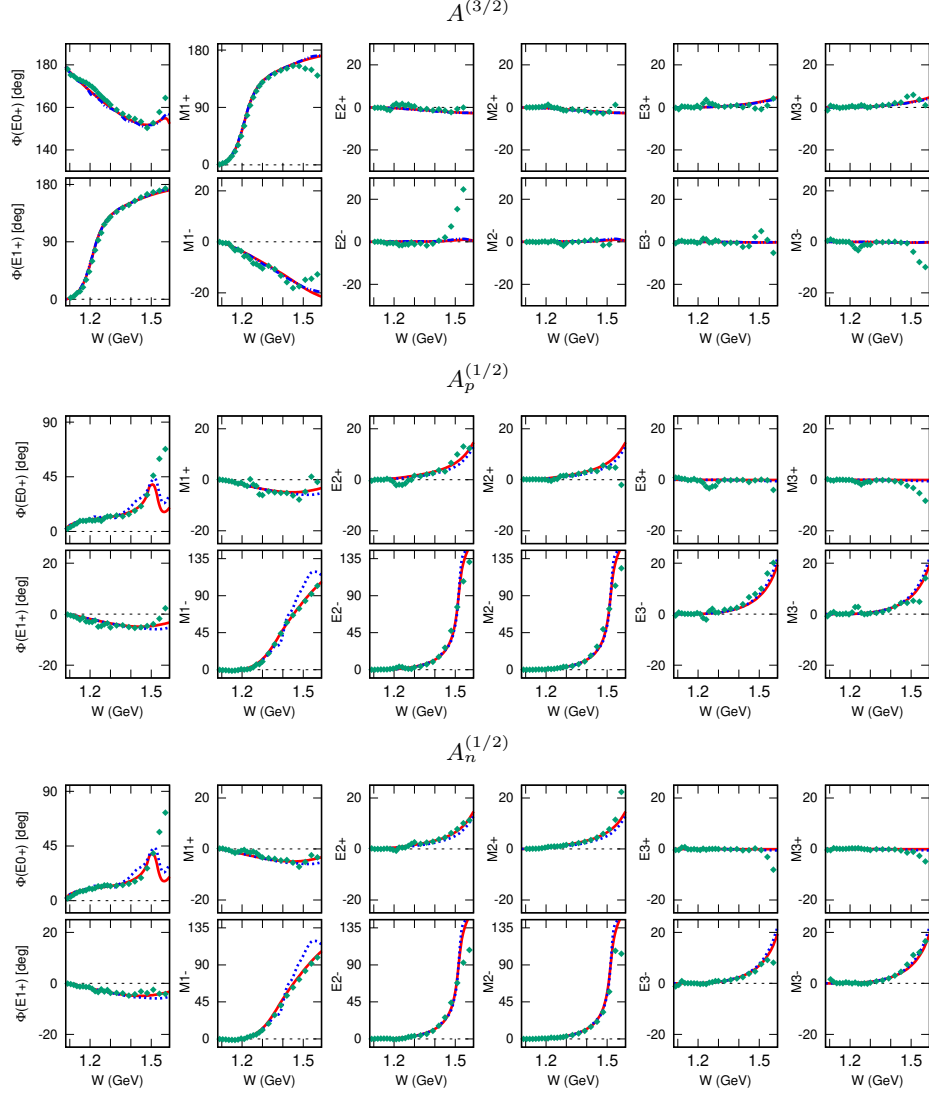


FIG. 29: Comparison between the SE multipole phases of pion photoproduction and pion-nucleon phases at low energies. Green points show the phases of the electric and magnetic multipoles of our final solution. The red and blue lines are pion nucleon phase shifts of KA84[62] and GWU/SAID[63], respectively, corresponding to the πN final states of the photoproduction multipoles. E.g. S_{11} corresponds to E_{0+} ($A_p^{(1/2)}$ and $A_n^{(1/2)}$), P_{33} to E_{1+} and M_{1+} , ($A^{(3/2)}$), etc. Note, in the Watson regime below 2π threshold, the phases should be identical, due to unitarity.

IV. SUMMARY AND CONCLUSIONS

Using the formalism introduced and explained for η photoproduction in Ref. [10], we have performed a fixed- t single-energy partial wave analysis of pion photoproduction in full isospin on the world collection of data. In an iterative two-step process the single-energy multipoles are constrained by fixed- t Pietarinen expansions fitted to experimental data. This leads to a partial wave expansion that obeys fixed- t analyticity with a least model dependence. In the energy range of $W = 1.09 - 2.20$ GeV we have obtained electric and magnetic multipoles $E_{\ell\pm}, M_{\ell\pm}$, up to F waves, $\ell = 3$, in 135 energy bins of about 5-10 MeV width. First we used randomized starting solutions from BnGa, SAID, and MAID energy dependent solutions and obtained three different SE solutions, SE1, SE2 and SE3 in an iterative procedure. These three SE solutions appeared already much closer together than the three underlying ED solutions, where we started from. Second we generated an ‘average’ SE solution, SEav, again in an iterative process. All four SE solutions compare very well with the experimental data, where the ‘averaged’ solution SEav is obtained in the least model dependent way. Finally, we compared our four SE solutions in their predictions for unmeasured polarization observables. At lower energies the spread of these predictions is rather small, but it becomes larger at higher energies, where it will help to propose new measurements in order to get a unique PWA.

ACKNOWLEDGMENTS

This work was supported by the Deutsche Forschungsgemeinschaft (SFB 1044).

APPENDICES

Appendix A: Kinematics in pion photoproduction

For pion photoproduction on the nucleon, we consider the reaction

$$\gamma(k) + N(p_i) \rightarrow \pi(q) + N'(p_f), \quad (\text{A1})$$

where the variables in brackets denote the four-momenta of the participating particles. In the pion-nucleon center-of-mass (c.m.) system, we define

$$k^\mu = (\omega_\gamma, \mathbf{k}), \quad q^\mu = (\omega_\pi, \mathbf{q}) \quad (\text{A2})$$

for photon and pion, and

$$p_i^\mu = (E_i, \mathbf{p}_i), \quad p_f^\mu = (E_f, \mathbf{p}_f) \quad (\text{A3})$$

for incoming and outgoing nucleon, respectively. The familiar Mandelstam variables are given as

$$s = W^2 = (p_i + k)^2, \quad t = (q - k)^2, \quad u = (p_f - k)^2, \quad (\text{A4})$$

the sum of the Mandelstam variables is given by the sum of the external masses

$$s + t + u = 2m_N^2 + m_\pi^2, \quad (\text{A5})$$

where m_N and m_π are masses of nucleon and pion, respectively. In the pion-nucleon center-of-mass system, the energies and momenta can be related to the Mandelstam variable s by

$$k = |\mathbf{k}| = \frac{s - m_N^2}{2\sqrt{s}}, \quad \omega = \frac{s + m_\pi^2 - m_N^2}{2\sqrt{s}}, \quad (\text{A6})$$

$$q = |\mathbf{q}| = \left[\left(\frac{s - m_\pi^2 + m_N^2}{2\sqrt{s}} \right) - m_N^2 \right]^{\frac{1}{2}}, \quad (\text{A7})$$

$$E_i = \frac{s - m_N^2}{2\sqrt{s}}, \quad E_f = \frac{s + m_\pi^2 + m_N^2}{2\sqrt{s}}, \quad (\text{A8})$$

$W = \sqrt{s}$ is the c.m. energy. Furthermore, we will also refer to the lab energy of the photon, $E = (s - m_N^2)/(2m_N)$.

Starting from the s -channel reaction $\gamma + N \Rightarrow \pi + N$, using crossing relation, one obtains two other channels:

$$\gamma + \pi \Rightarrow N + \bar{N} \quad t\text{-channel}, \quad (\text{A9})$$

$$\gamma + \bar{N} \Rightarrow \pi + \bar{N} \quad u\text{-channel}. \quad (\text{A10})$$

All three channels defined above are described by a set of four invariant amplitudes. The singularities of the invariant amplitudes are defined by unitarity in s , u and t channels:

$$s\text{-channel cut: } (m_N + m_\pi)^2 \leq s < \infty, \quad (\text{A11})$$

$$u\text{-channel cut: } (m_N + m_\pi)^2 \leq u < \infty, \quad (\text{A12})$$

and nucleon poles at $s = m_N^2$, $u = m_N^2$. The crossing symmetrical variable is

$$\nu = \frac{s - u}{4m_N}. \quad (\text{A13})$$

The s -channel region is shown in Fig. 30. The upper and lower boundaries of the physical region are given by the scattering angles $\theta = 0$ and $\theta = 180^\circ$, respectively. The c.m. energy W and the c.m. scattering angle θ can be obtained from the variables ν and t by

$$W^2 = m_N(m_N + 2\nu) - \frac{1}{2}(t - m_\pi^2) \quad (\text{A14})$$

and

$$\cos \theta = \frac{t - m_\pi^2 + 2k\omega}{2kq}. \quad (\text{A15})$$

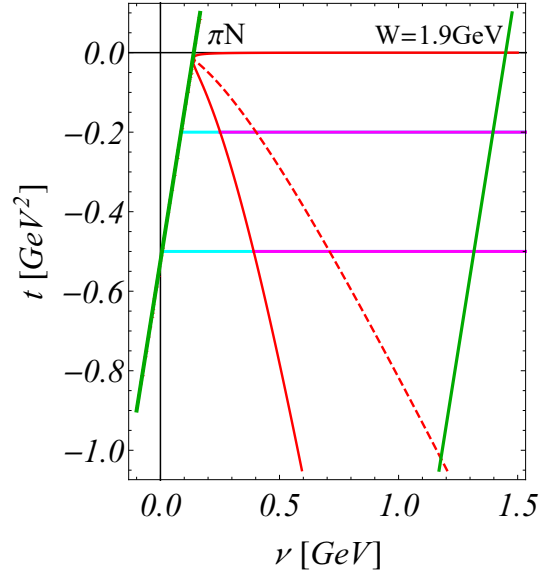


FIG. 30: The Mandelstam plane for pion photoproduction on the nucleon. The red solid curves are the boundaries of the physical region from $\theta = 0$ to $\theta = 180^\circ$ and the red dashed line shows $\theta = 90^\circ$. The green tilted vertical lines are the threshold for pion production at $W = 1.073$ GeV, and $W = 1.9$ GeV. The horizontal lines denote the t -values -0.2 , -0.5 GeV², where detailed results for observables and amplitudes are shown and discussed in the text, Fig. 6-9. The magenta parts give the part inside the physical region, whereas the cyan parts indicate non-zero amplitudes in the unphysical region. The fixed- t lines enter the physical region at $W = 1.208$ GeV ($t = -0.2$ GeV²) and $W = 1.369$ GeV ($t = -0.5$ GeV²).

Appendix B: Cross section and polarization observables

Experiments with three types of polarization can be performed in meson photoproduction: photon beam polarization, polarization of the target nucleon and recoil nucleon polarization detection. Target polarization will be described in the frame $\{x, y, z\}$ in Fig. 31, with the z -axis pointing into the direction of the photon momentum $\hat{\mathbf{k}}$, the y -axis perpendicular to the reaction plane, $\hat{\mathbf{y}} = \hat{\mathbf{k}} \times \hat{\mathbf{q}} / \sin \theta$, and the x -axis given by $\hat{\mathbf{x}} = \hat{\mathbf{y}} \times \hat{\mathbf{z}}$. For recoil polarization we will use the frame $\{x', y', z'\}$, with the z' -axis defined by the momentum vector of the outgoing meson $\hat{\mathbf{q}}$, the y' -axis as for target polarization and the x' -axis given by $\hat{\mathbf{x}}' = \hat{\mathbf{y}}' \times \hat{\mathbf{z}}'$.

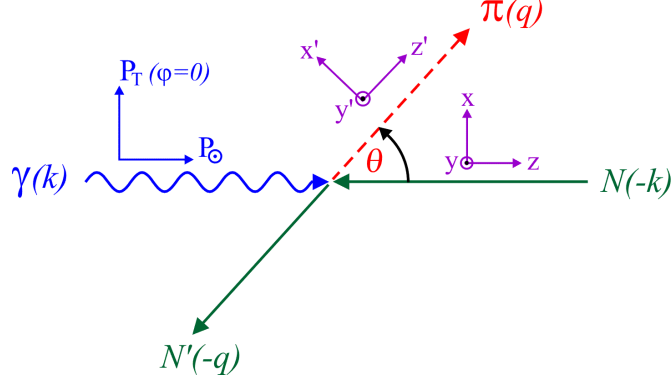


FIG. 31: Kinematics of photoproduction and frames for polarization. The frame $\{x, y, z\}$ is used for target polarization $\{P_x, P_y, P_z\}$, whereas the recoil polarization $\{P_{x'}, P_{y'}, P_{z'}\}$ is defined in the frame $\{x', y', z'\}$, which is rotated around $y' = y$ by the polar angle θ . The azimuthal angle φ is defined in the $\{x, y\}$ plane and is zero in the projection shown in the figure.

The photon polarization can be linear or circular. For a linear photon polarization ($P_T = 1$) in the reaction plane $\hat{\mathbf{x}}$ we get $\varphi = 0$ and perpendicular, in direction $\hat{\mathbf{y}}$, the polarization angle is $\varphi = \pi/2$. For right-handed circular polarization $P_\odot = +1$. We may classify the differential cross sections by the three classes of double polarization experiments and one class of triple polarization experiments, which, however, do not give additional information:

- polarized photons and polarized target

$$\begin{aligned} \frac{d\sigma}{d\Omega} = \sigma_0 \{ & 1 - P_T \Sigma \cos 2\varphi \\ & + P_x (-P_T H \sin 2\varphi + P_\odot F) \\ & + P_y (T - P_T P \cos 2\varphi) \\ & + P_z (P_T G \sin 2\varphi - P_\odot E) \} , \end{aligned} \quad (\text{B1})$$

- polarized photons and recoil polarization

$$\begin{aligned} \frac{d\sigma}{d\Omega} = \sigma_0 \{ & 1 - P_T \Sigma \cos 2\varphi \\ & + P_{x'} (-P_T O_{x'} \sin 2\varphi - P_\odot C_{x'}) \\ & + P_{y'} (P - P_T T \cos 2\varphi) \\ & + P_{z'} (-P_T O_{z'} \sin 2\varphi - P_\odot C_{z'}) \} , \end{aligned} \quad (\text{B2})$$

- polarized target and recoil polarization

$$\begin{aligned} \frac{d\sigma}{d\Omega} = \sigma_0 \{ & 1 + P_y T + P_{y'} P + P_{x'} (P_x T_{x'} - P_z L_{x'}) \\ & + P_{y'} P_y \Sigma + P_{z'} (P_x T_{z'} + P_z L_{z'}) \} . \end{aligned} \quad (\text{B3})$$

In these equations σ_0 denotes the unpolarized differential cross section, the transverse degree of photon polarization is denoted by P_T , P_\odot is the right-handed circular photon polarization and φ the azimuthal angle of the photon polarization vector in respect to the reaction plane. Instead of asymmetries, in the following we will often discuss the product of the unpolarized cross section with the asymmetries and will use the notation $\tilde{\Sigma} = \sigma_0 \Sigma, \tilde{T} = \sigma_0 T, \dots$. In appendix C we give expressions of the observables in terms of CGLN and helicity amplitudes.

Appendix C: Observables expressed in CGLN and helicity amplitudes

Spin observables expressed in CGLN amplitudes are given by:

$$\sigma_0 = \text{Re} \{ F_1^* F_1 + F_2^* F_2 + \sin^2 \theta (F_3^* F_3 / 2 + F_4^* F_4 / 2 + F_2^* F_3 + F_1^* F_4 + \cos \theta F_3^* F_4) - 2 \cos \theta F_1^* F_2 \} \rho \quad (\text{C1})$$

$$\check{\Sigma} = -\sin^2 \theta \text{Re} \{ (F_3^* F_3 + F_4^* F_4) / 2 + F_2^* F_3 + F_1^* F_4 + \cos \theta F_3^* F_4 \} \rho \quad (\text{C2})$$

$$\check{T} = \sin \theta \text{Im} \{ F_1^* F_3 - F_2^* F_4 + \cos \theta (F_1^* F_4 - F_2^* F_3) - \sin^2 \theta F_3^* F_4 \} \rho \quad (\text{C3})$$

$$\check{P} = -\sin \theta \text{Im} \{ 2F_1^* F_2 + F_1^* F_3 - F_2^* F_4 - \cos \theta (F_2^* F_3 - F_1^* F_4) - \sin^2 \theta F_3^* F_4 \} \rho \quad (\text{C4})$$

$$\check{E} = \text{Re} \{ F_1^* F_1 + F_2^* F_2 - 2 \cos \theta F_1^* F_2 + \sin^2 \theta (F_2^* F_3 + F_1^* F_4) \} \rho \quad (\text{C5})$$

$$\check{F} = \sin \theta \text{Re} \{ F_1^* F_3 - F_2^* F_4 - \cos \theta (F_2^* F_3 - F_1^* F_4) \} \rho \quad (\text{C6})$$

$$\check{G} = \sin^2 \theta \text{Im} \{ F_2^* F_3 + F_1^* F_4 \} \rho \quad (\text{C7})$$

$$\check{H} = \sin \theta \text{Im} \{ 2F_1^* F_2 + F_1^* F_3 - F_2^* F_4 + \cos \theta (F_1^* F_4 - F_2^* F_3) \} \rho \quad (\text{C8})$$

$$\check{O}_{x'} = \sin \theta \text{Re} \{ F_1^* F_1 - F_2^* F_2 - F_2^* F_3 + F_1^* F_4 - \cos \theta (F_2^* F_4 - F_1^* F_3) \} \rho \quad (\text{C9})$$

$$\check{O}_{z'} = \text{Re} \{ 2F_1^* F_2 - \cos \theta (F_1^* F_1 + F_2^* F_2) + \sin^2 \theta (F_1^* F_3 + F_2^* F_4) \} \rho \quad (\text{C10})$$

$$\check{O}_{x'} = \sin \theta \text{Im} \{ F_2^* F_3 - F_1^* F_4 + \cos \theta (F_2^* F_4 - F_1^* F_3) \} \rho \quad (\text{C11})$$

$$\check{O}_{z'} = -\sin^2 \theta \text{Im} \{ F_1^* F_3 + F_2^* F_4 \} \rho \quad (\text{C12})$$

$$\check{L}_{x'} = -\sin \theta \text{Re} \{ F_1^* F_1 - F_2^* F_2 - F_2^* F_3 + F_1^* F_4 + \sin^2 \theta (F_4^* F_4 - F_3^* F_3) / 2 + \cos \theta (F_1^* F_3 - F_2^* F_4) \} \rho \quad (\text{C13})$$

$$\check{L}_{z'} = \text{Re} \{ 2F_1^* F_2 - \cos \theta (F_1^* F_1 + F_2^* F_2) + \sin^2 \theta (F_1^* F_3 + F_2^* F_4 + F_3^* F_4) + \cos \theta \sin^2 \theta (F_3^* F_3 + F_4^* F_4) / 2 \} \rho \quad (\text{C14})$$

$$\check{T}_{x'} = -\sin^2 \theta \text{Re} \{ F_1^* F_3 + F_2^* F_4 + F_3^* F_4 + \cos \theta (F_3^* F_3 + F_4^* F_4) / 2 \} \rho \quad (\text{C15})$$

$$\check{T}_{z'} = \sin \theta \text{Re} \{ F_1^* F_4 - F_2^* F_3 + \cos \theta (F_1^* F_3 - F_2^* F_4) + \sin^2 \theta (F_4^* F_4 - F_3^* F_3) / 2 \} \rho \quad (\text{C16})$$

$$\text{with } \check{\Sigma} = \Sigma \sigma_0 \text{ etc. and } \rho = q/k. \quad (\text{C17})$$

The 16 polarization observables of pseudoscalar photoproduction fall into four groups, single spin with unpolarized cross section included, beam-target, beam-recoil and target-recoil observables. The simplest representation of these observables is given in terms of helicity amplitudes, see Table V.

TABLE V: Spin observables expressed by helicity amplitudes in the notation of Barker [64] and Walker [65]. A phase space factor q/k has been omitted in all expressions. The differential cross section is given by σ_0 and the spin observables \check{O}_i are obtained from the spin asymmetries A_i by $\check{O}_i = A_i \sigma_0$.

Observable	Helicity Representation	Type
σ_0	$\frac{1}{2}(H_1 ^2 + H_2 ^2 + H_3 ^2 + H_4 ^2)$	\mathcal{S} (single spin)
$\check{\Sigma}$	$\text{Re}(H_1 H_4^* - H_2 H_3^*)$	
\check{T}	$\text{Im}(H_1 H_2^* + H_3 H_4^*)$	
\check{P}	$-\text{Im}(H_1 H_3^* + H_2 H_4^*)$	
\check{G}	$-\text{Im}(H_1 H_4^* + H_2 H_3^*)$	\mathcal{BT} (beam-target)
\check{H}	$-\text{Im}(H_1 H_3^* - H_2 H_4^*)$	
\check{E}	$\frac{1}{2}(- H_1 ^2 + H_2 ^2 - H_3 ^2 + H_4 ^2)$	
\check{F}	$\text{Re}(H_1 H_2^* + H_3 H_4^*)$	
$\check{O}_{x'}$	$-\text{Im}(H_1 H_2^* - H_3 H_4^*)$	\mathcal{BR} (beam-recoil)
$\check{O}_{z'}$	$\text{Im}(H_1 H_4^* - H_2 H_3^*)$	
$\check{C}_{x'}$	$-\text{Re}(H_1 H_3^* + H_2 H_4^*)$	
$\check{C}_{z'}$	$\frac{1}{2}(- H_1 ^2 - H_2 ^2 + H_3 ^2 + H_4 ^2)$	
$\check{T}_{x'}$	$\text{Re}(H_1 H_4^* + H_2 H_3^*)$	\mathcal{TR} (target-recoil)
$\check{T}_{z'}$	$\text{Re}(H_1 H_2^* - H_3 H_4^*)$	
$\check{L}_{x'}$	$-\text{Re}(H_1 H_3^* - H_2 H_4^*)$	
$\check{L}_{z'}$	$\frac{1}{2}(H_1 ^2 - H_2 ^2 - H_3 ^2 + H_4 ^2)$	

Appendix D: Isospin decomposition of amplitudes and multipoles

Invariant amplitudes in pion photoproduction may be decomposed into the isospin combinations $A_i^I (I = +, -, 0)$, where $A_i^{(+,-)}$ describe absorption of isovector γ quant, while $A_i^{(0)}$ describes absorption of isoscalar one. The physical photoproduction amplitudes are obtained as follows:

$$\begin{aligned} A_{\pi+n} &= \sqrt{2}(A^{(-)} + A^{(0)}), \\ A_{\pi-p} &= -\sqrt{2}(A^{(-)} - A^{(0)}), \\ A_{\pi^0 p} &= A^{(+)} + A^{(0)}, \\ A_{\pi^0 n} &= A^{(+)} - A^{(0)}. \end{aligned} \quad (\text{D1})$$

Amplitudes $A_i^{(+,-,0)}$ are crossing symmetric or crossing antisymmetric:

$$A_i^I(\nu, t) = \epsilon^I \xi_i A_i^I(-\nu, t), \quad (\text{D2})$$

$$\epsilon^+ = \epsilon^0 = -\epsilon^- = 1, \quad \xi_1 = \xi_2 = -\xi_8 = \xi_6 = 1.$$

In SE PWA, when resonances of the πN system are analyzed in terms of definite isospin $I = 1/2$ or $3/2$, one has to use amplitudes describing the πN system in the final state with isospin $1/2$ or $3/2$.

$$\begin{aligned} A^{(3/2)} &= A^{(+)} - A^{(-)}, \quad I = \frac{3}{2}, \\ A^{(1/2)} &= A^{(+)} + 2A^{(-)}, \quad I = \frac{1}{2}, \\ &A^{(0)}, \quad I = \frac{1}{2}. \end{aligned} \quad (\text{D3})$$

In the isospin $I = \frac{1}{2}$ channel it is common to use the combination

$$A_p^{(1/2)} = A^{(0)} + \frac{1}{3}A^{(1/2)}, \quad A_n^{(1/2)} = A^{(0)} - \frac{1}{3}A^{(1/2)}, \quad (\text{D4})$$

where $p(n)$ denotes proton (neutron) target.

Finally, the isospin combinations $(+, -, 0)$ can be expressed into charge and isospin amplitudes as

$$A^{(+)} = \frac{1}{2}(A_{\pi^0 p} + A_{\pi^0 n}) = \frac{1}{2}(A_p^{(1/2)} + A_n^{(1/2)}) + \frac{2}{3}A^{(3/2)}, \quad (\text{D5})$$

$$A^{(-)} = \frac{1}{2\sqrt{2}}(A_{\pi+n} - A_{\pi-p}) = \frac{1}{2}(A_p^{(1/2)} - A_n^{(1/2)}) - \frac{1}{3}A^{(3/2)}, \quad (\text{D6})$$

$$A^{(0)} = \frac{1}{2}(A_{\pi^0 p} - A_{\pi^0 n}) = \frac{1}{2\sqrt{2}}(A_{\pi+n} + A_{\pi-p}) = \frac{1}{2}(A_p^{(1/2)} - A_n^{(1/2)}). \quad (\text{D7})$$

-
- [1] A. V. Anisovich *et al.*, Phys. Rev. C **96**, 055202 (2017), and references therein; and <http://pwa.hiskp.uni-bonn.de/>.
- [2] D. Rönchen, M. Döring, H. Haberzettl, J. Haidenbauer, U. -G. Meißner and K. Nakayama Eur. Phys. J. A **51**, 70 (2015), and references therein; and <http://collaborations.fz-juelich.de/ikp/meson-baryon/main>.
- [3] R. L. Workman, R. A. Arndt, W. J. Briscoe, M. W. Paris, and I. I. Strakovsky, Phys. Rev. C **86**, 035202 (2012); and <http://gwdac.phys.gwu.edu/>.
- [4] D. Drechsel, S. S. Kamalov and L. Tiator, Eur. Phys. J. A **34** (2007) 69; and <https://maid.kph.uni-mainz.de/>.
- [5] A. V. Anisovich *et al.*, Eur. Phys. J. A **52**, no. 9, 284 (2016).
- [6] A. S. Omelaenko, Yad. Fiz. **34**, 730 (1981).
- [7] Y. Wunderlich, A. Švarc, R. L. Workman, L. Tiator and R. Beck, Phys. Rev. C **96**, no. 6, 065202 (2017).
- [8] R. L. Workman, L. Tiator, Y. Wunderlich, M. Döring and H. Haberzettl, Phys. Rev. C **95**, no. 1, 015206 (2017).
- [9] A. Švarc, Y. Wunderlich, H. Osmanović, M. Hadžimehmedović, R. Omerović, J. Stahov, V. Kashevarov, K. Nikonov, M. Ostrick, L. Tiator, and R. Workman, Phys. Rev. C **97**, 054611 (2018).
- [10] H. Osmanović, M. Hadžimehmedović, R. Omerović, J. Stahov, V. Kashevarov, K. Nikonov, M. Ostrick, L. Tiator, and A. Švarc, Phys. Rev. C **97**, 015207 (2018).
- [11] H. Osmanović, M. Hadžimehmedović, R. Omerović, J. Stahov, M. Gortchein, V. Kashevarov, K. Nikonov, M. Ostrick, L. Tiator, and A. Švarc, Phys. Rev. C **100**, 055203 (2019).
- [12] K. M. Watson, Phys. Rev. **95**, 228 (1954).
- [13] G. Höhler, *Pion Nucleon Scattering*, Part 2, Landolt-Börnstein: Elastic and Charge Exchange Scattering of Elementary Particles, Vol. 9b (Springer-Verlag, Berlin, 1983).
- [14] K. M. Watson, Phys. Rev. **88**, 1163 (1952).
- [15] GWU website: <https://gwdac.phys.gwu.edu/>
- [16] D. Hornidge *et al.* (A2 Collaboration at MAMI), Phys. Rev. Lett. **111**, no. 6, 062004 (2013).
- [17] P. Adlarson *et al.* (A2 Collaboration at MAMI), Phys. Rev. C **92**, 024617 (2015).
- [18] M. Dugger *et al.* (CLAS Collaboration), Phys. Rev. C **76**, 025211 (2007).
- [19] V. Crede *et al.* (CBELSA/TAPS Collaboration), Phys. Rev. C **84**, 055203 (2011).
- [20] R. Beck *et al.* (A2 Collaboration at MAMI), Eur. Phys. J. A **28**, 173 (2006).
- [21] O. Bartalini *et al.* (GRAAL Collaboration), Eur. Phys. J. A **26**, 399 (2005).
- [22] N. Sparks *et al.* (CBELSA/TAPS Collaboration), Phys. Rev. C **81**, 065210 (2010).
- [23] G. Barbiellini *et al.*, Phys. Rev. **184**, 1402 (1969);
V. G. Gorbenko *et al.*, Pisma Zh. Eksp. Teor. Fiz. **19**, 659 (1974);
V. G. Gorbenko *et al.*, Yad. Fiz. **27**, 1204 (1978);
A. A. Belyaev *et al.*, Nucl. Phys. B **213**, 201 (1983);
G. Blanpied *et al.*, Phys. Rev. Lett. **69**, 1880 (1992);
R. Beck *et al.*, Phys. Rev. Lett. **78**, 606 (1997);
F. V. Adamian *et al.*, Phys. Rev. C **63**, 054606 (2001).
- [24] S. Schumann *et al.* (A2 Collaboration at MAMI), Phys. Lett. B **750**, 252 (2015).
- [25] J. R. M. Annand *et al.* (A2 Collaboration at MAMI), Phys. Rev. C **93**, 055209 (2016).
- [26] J. Hartmann *et al.* (CBELSA/TAPS Collaboration), Phys. Rev. Lett. **113**, 062001 (2014).
- [27] P. Feller *et al.*, Nucl. Phys. B **110**, 397 (1976);
V. G. Gorbenko *et al.*, Yad. Fiz. **26**, 320 (1977);
P. S. L. Booth *et al.*, Nucl. Phys. B **121**, 45 (1977);
H. Herr *et al.*, Nucl. Phys. B **125**, 157 (1977);
M. Fukushima *et al.*, Nucl. Phys. B **136**, 189 (1978);
P. J. Bussey *et al.*, Nucl. Phys. B **154**, 492 (1979);
M. M. Asaturian *et al.*, JETP Lett. **44**, 341 (1986);
K. S. Agababian *et al.*, Yad. Fiz. **50**, 1341 (1989);
A. Bock *et al.*, Phys. Rev. Lett. **81**, 534 (1998).
- [28] V. G. Gorbenko *et al.*, Pisma Zh. Eksp. Teor. Fiz. **22**, 393 (1975);
S. Kato *et al.*, Nucl. Phys. B **168**, 1 (1980);
A. S. Bratashevsky *et al.*, Nucl. Phys. B **166**, 525 (1980).
- [29] J. Linturi, PhD thesis, Mainz University (2015).
- [30] M. Gottschall *et al.* (CBELSA/TAPS Collaboration), Phys. Rev. Lett. **112**, 012003 (2014).
- [31] P. Otte, PhD thesis, Mainz University (2015).
- [32] J. Ahrens *et al.*, Eur. Phys. J. A **26**, 135 (2005).
- [33] A. Thiel *et al.* (CBELSA/TAPS Collaboration), Phys. Rev. Lett. **109**, 102001 (2012).
- [34] P. J. Bussey *et al.*, Nucl. Phys. B **159**, 383 (1979).
- [35] J. Ahrens *et al.*, Eur. Phys. J. A **21**, 323 (2004).
- [36] J. Ahrens *et al.*, Phys. Rev. C **74**, 045204 (2006).
- [37] M. Dugger *et al.*, Phys. Rev. C **79**, 065206 (2009).
- [38] S. D. Ecklund, R. L. Walker, Phys. Rev. **159**, 1195 (1967);
C. Betourne *et al.*, Phys. Rev. **172**, 1343 (1968);

- B. Bouquet *et al.*, Phys. Rev. Lett. **27**, 1244 (1971);
 K. Ekstrand *et al.*, Phys. Rev. D **6**, 1 (1972);
 T. Fujii *et al.*, Nucl. Phys. B **120**, 395 (1977);
 I. Arai *et al.*, J. Phys. Soc. Jap. **43**, 363 (1977);
 K. H. Althoff *et al.*, Z. Phys. C **18**, 199 (1983);
 K. Buechler *et al.*, Nucl. Phys. A **570**, 580 (1994);
 H. W. Dannhausen *et al.*, Eur.Phys.J. A **11**, 441 (2001).
- [39] R. E. Taylor, R. F. Mozley, Phys. Rev. **117**, 835 (1960);
 R. C. Smith, R. F. Mozley, Phys. Rev. **130**, 2429 (1963);
 G. Knies *et al.*, Phys. Rev. D **10**, 2778 (1974);
 V. B. Ganenko *et al.*, Sov. J. Nucl. Phys. **23**, 162 (1976);
 R. Beck *et al.*, Phys.Rev. C **61**, 035204 (2000);
 J. Ajaka *et al.*, Phys. Lett. B **475**, 372 (2000);
 G. Blanpied *et al.*, Phys. Rev. C **64**, 025203 (2001).
- [40] O. Bartalini *et al.* (GRAAL Collaboration), Phys. Lett. B **544**, 113 (2002).
- [41] M. Dugger *et al.* (CLAS Collaboration), Phys. Rev. C **88**, 065203 (2013); Phys.Rev. C **89**, 029901 (2014).
- [42] S. Arai *et al.*, Nucl. Phys. B **48**, 397 (1972);
 P. Feller *et al.*, Nucl. Phys. B **102**, 207 (1976);
 M. Fukushima *et al.*, Nucl. Phys. B **130**, 486 (1977);
 K. Fujii *et al.*, Nucl. Phys. B **197**, 365 (1982);
 K. H. Althoff *et al.*, Nucl. Phys. B **53**, 9 (1973);
 K. H. Althoff *et al.*, Phys. Lett. B **59**, 93 (1975);
 K. H. Althoff *et al.*, Phys. Lett. B **63**, 107 (1976);
 K. H. Althoff *et al.*, Nucl. Phys. B **131**, 1 (1977);
 H. Dutz *et al.*, Nucl. Phys. A **601**, 319 (1996);
 V. A. Getman *et al.*, Sov. J. Nucl. Phys. **31**, 480 (1980).
- [43] P. J. Bussey *et al.*, Nucl. Phys. B **154**, 205 (1979);
 K. Egawa *et al.*, Nucl. Phys. B **188**, 11 (1981);
 V. A. Getman *et al.*, Nucl. Phys. B **188**, 397 (1981).
- [44] A. A. Belyaev *et al.*, Sov. J. Nucl. Phys. **40**, 83 (1984);
 J. Ahrens *et al.*, Eur. Phys. J. A **26**, 135 (2005).
- [45] P. J. Bussey *et al.*, Nucl. Phys. B **169**, 403 (1980);
 A. A. Belyaev *et al.*, Yad. Fiz. **43**, 1469 (1986).
- [46] G. Neugebauer *et al.*, Phys. Rev. **119**, 1726 (1960);
 P. E. Scheffler, P.L.Walden, Nucl. Phys. B **75**, 125 (1974);
 M. Beneventano *et al.*, Nuovo Cim. A **19**, 529 (1974);
 G. von Holtey *et al.*, Nucl. Phys. B **70**, 379 (1974);
 T. Fujii *et al.*, Phys. Rev. Lett. **26**, 1672 (1971);
 P. E. Argan *et al.*, Nucl. Phys. A **296**, 373 (1978).
- [47] V. Rossi *et al.*, Nuovo Cim. A **13**, 59 (1973);
 P. Benz *et al.*, Nucl. Phys. B **65**, 158 (1973);
 J. C. Comiso *et al.*, Phys. Rev. D **12**, 719 (1975);
 A. L. Weiss *et al.*, Nucl. Phys. B **101**, 1 (1975);
 M. T. Tran *et al.*, Nucl. Phys. A **324**, 301 (1979);
 R. Bagheri *et al.*, Phys. Rev. C **38**, 875 (1988);
 A. Shafi *et al.*, Phys. Rev. C **70**, 035204 (2004).
- [48] B. Briscoe *et al.* (A2 Collaboration at MAMI), Phys. Rev. C **86**, 065207 (2012).
- [49] W. Chen *et al.*(CLAS Collaboration), Phys. Rev. C **86**, 015206 (2012).
- [50] F. F. Liu *et al.*, Phys. Rev. B **136**, 1183 (1964).
 J. Alspector *et al.*, Phys. Rev. Lett. **28**, 1403 (1972).
 K. Kondo *et al.*, Phys. Rev. D **9**, 529 (1974).
 G. Knies *et al.*, Phys. Rev. D **10**, 2778 (1974).
 V. B. Ganenko *et al.*, Sov. J. Nucl. Phys. **23**, 511 (1976).
 L. O. Abrahamian *et al.*, Sov. J. Nucl. Phys. **32**, 69 (1980).
 F. V. Adamian *et al.*, J. Phys. G **15**, 1797 (1989).
- [51] G. Mandaglio *et al.* (GRAAL Collaboration), Phys. Rev. C **82**, 045209 (2010).
- [52] K. H. Althoff *et al.*, Nucl. Phys. B **96**, 497 (1975);
 K. H. Althoff *et al.*, Nucl. Phys. B **116**, 253 (1976);
 K. H. Althoff *et al.*, Nucl. Phys. B **131**, 1 (1977);
 K. Fujii *et al.*, Nucl. Phys. B **187**, 53 (1981).
- [53] J. P. Kenemuth, P. C. Stein, Phys. Rev. **129**, 2259 (1963);
 H. Takeda *et al.*, Nucl. Phys. B **168**, 17 (1980);
 J. C. Alder *et al.*, Phys. Rev. D **27**, 1040 (1983);
 G. J. Kim *et al.*, Phys. Rev. D **43**, 687 (1991);

- J. C. Stasko *et al.*, Phys. Rev. Lett. **72**, 973 (1994).
- [54] W. J. Briscoe *et al.* (A2 Collaboration at MAMI), Phys. Rev. C **100**, 065205 (2019).
- [55] M. Dieterle *et al.* (A2 Collaboration at MAMI), Phys. Rev. C **97**, 065205 (2018).
- [56] Clinesmith, PhD thesis, CIT (1967);
C. Bacciet *et al.*, Phys. Lett. C **39**, 559 (1972);
Y. Hemmiet *et al.*, Nucl. Phys. B **55**, 333 (1973);
A. Ando *et al.*, Physik Daten, Fachinformationszentrum, Karlsruhe (1977).
- [57] R. Di Salvo *et al.* (GRAAL Collaboration), Eur. Phys. J. A **42**, 151 (2009)
- [58] M. Dieterle *et al.* (A2 Collaboration at MAMI), Phys. Lett. B **770**, 523 (2017).
- [59] P. Adlarson *et al.* [A2 Collaboration at MAMI], Phys. Rev. C **92**, 024617 (2015).
- [60] C. de Boor, *A Practical Guide to Splines*, Springer-Verlag, Heidelberg, 1978, revised 2001.
- [61] W. J. Briscoe *et al.* (A2 Collaboration at MAMI), Phys. Rev. C **100**, no.6, 065205 (2019).
- [62] R. Koch, Z. Physik C **29**, 597 (1985);
R. Koch, Nucl. Phys. A **448**, 707 (1986).
- [63] R. A. Arndt, W. J. Briscoe, I. I. Strakovsky, and R. L. Workman, Phys. Rev. C **74**, 045205 (2006).
- [64] I. S. Barker, A. Donnachie, J. K. Storrow, Nucl. Phys. B **95**, 347 (1975).
- [65] R. L. Walker, Phys. Rev. **182**, 1729 (1969).